

ARTICLE

Pre- and post-yield bond, tension-stiffening, and cracking in ultra-high performance fiber reinforced concrete

Alexander B. Sturm¹  | Phillip Visintin² 

¹Department of Civil Engineering, National Cheng Kung University, Taiwan

²School of Civil, Environmental and Mining Engineering, The University of Adelaide, Adelaide, South Australia, Australia

Correspondence

Phillip Visintin, School of Civil, Environmental and Mining Engineering, The University of Adelaide, Adelaide, South Australia 5005, Australia.
Email: phillip.visintin@adelaide.edu.au

Funding information

Australian Research Council, Grant/Award Number: DP190102650

Abstract

In reinforced concrete elements, tension-stiffening strongly influences deflections and crack-widths at the serviceability limit, and plastic hinge rotation at the ultimate limit. Modeling has shown the impact of tension-stiffening at the ultimate limit to be particularly important when ultimate failure is governed by reinforcement rupture, which has been common in ultra-high performance fiber reinforced concrete (UHPFRC) elements. It is further known that the magnitude of tension-stiffening and crack opening is proportional to both the reinforcement ratio of the tension chord and the diameter of the reinforcing bar. Despite this understanding, very little testing has been undertaken to quantify the bond between larger diameter reinforcement and UHPFRC and also on the resulting impact to tension-stiffening and concrete cracking. To address these issues, in this paper a series of bond and tension-stiffening tests are undertaken on ultra-high performance concretes both with and without steel fibers. The result of the experiments is used to develop a local bond stress slip relationship applicable to both pre- and post-yield. When implemented in a partial-interaction model, it is shown that the new bond model can be used to predict pre- and post-yield tension-stiffening and crack-widths.

KEYWORDS

bond, FRC, tension-stiffening cracking, UHPC, UHPFRC

1 | INTRODUCTION

In a cracked region of reinforced concrete, partial-interaction mechanics describe the distribution of concrete and reinforcement tensile stresses between cracks and the relative displacements between the materials.¹⁻³ The

degree of partial-interaction between the materials has the effect of reducing the average strain in the reinforcement and increasing the average strain in the concrete between cracks.^{4,5} At the serviceability limit state, it is well recognized that an understanding of this partial-interaction behavior is therefore essential to achieve an accurate prediction of member deflection and crack-width.^{6,7} The importance of partial-interaction is however less well recognized at the ultimate limit-state. Despite being less recognized it is equally important, because if ignored, reinforcement strains, hinge rotation, and member

Discussion on this paper must be submitted within two months of the print publication. The discussion will then be published in print, along with the authors' closure, if any, approximately nine months after the print publication.

This is an open access article under the terms of the [Creative Commons Attribution-NonCommercial](https://creativecommons.org/licenses/by-nc/4.0/) License, which permits use, distribution and reproduction in any medium, provided the original work is properly cited and is not used for commercial purposes.

© 2022 The Authors. *Structural Concrete* published by John Wiley & Sons Ltd on behalf of International Federation for Structural Concrete.

ductility are all overestimated.⁵ This overestimate has been shown to be particularly important when quantifying the ductility of ultra-high performance fiber reinforced concrete (UHPFRC) flexural members, which commonly fail, by reinforcement rupture.^{8,9} Analogous findings were also reported by Moreno et al.¹⁰ who found that the average strains in tension-stiffening specimens at the fracture of the reinforcement were significantly lower than the fracture strain of the reinforcement for specimens with fibers.

To address the need to quantify post-yield partial-interaction behavior in UHPFRC elements, in this paper the results of a series of pull-out and tension-stiffening tests are reported. These results are then used as the basis for the development of a post-yield bond model, which is applied to predict tension-stiffening and crack-width from first loading to reinforcement rupture.

Previous studies investigating tension-stiffening of reinforced UHPFRC include those conducted by Jungwirth and Muttoni,¹¹ Oesterlee,¹² Visintin et al.,¹³ Hung et al.,¹⁴ and Khorami et al.¹⁵ which are summarized in Table 1. From this overview it is observed that very few studies have been conducted on specimens with bar diameter greater than 16 mm,^{11,14} and that when larger bar diameters are considered, the cross-sectional

dimensions have remained constant. This is important because it is widely accepted that crack-spacing and therefore crack-width is dependent on both bar diameter and reinforcement ratio,^{16–18} and based on existing test results these parameters cannot be uncoupled. Given the impact of bar diameter on cracking behavior, it is therefore also important that testing be conducted on larger diameter reinforcing bars given that these are commonly used in the construction of full-scale elements.

Given tension-stiffening is proportional to the local bond stress/slip (τ_b - δ) material properties, let us now also consider previous experimental research aimed at quantifying this property. In order to regress a generic τ_b - δ material property, Sturm and Visintin¹⁹ compiled a database of 203 pull-out test results conducted on UHPFRC. The range of parameters contained in the database is summarized in Table 2 where it can be seen that only eight of the existing 203 tests have been conducted on bars with a diameter exceeding 20 mm and the reinforcement cover is generally large. This is significant since the τ_b - δ relationship that governs partial-interaction behavior is a function of concrete cover thickness,^{17,21} and it has also been observed in tests on conventional concrete that bar diameter also influences behavior.^{22,23}

TABLE 1 Summary of geometric and material properties of UHPFRC tension-stiffening tests

Reference	<i>N</i>	<i>f_c</i>	<i>V_f</i> (%)	Fiber type	<i>l_f</i> (mm)	<i>d_f</i> (mm)	Specimen size	<i>d_b</i> (mm)	ρ (%)
Jungwirth and Muttoni ¹¹	3	199	2.5	Straight	20	0.3	150 × 150	12, 16 or 20	1–4.1
Oesterlee ¹²	12	198	3	Straight	13	0.6	200 × 50	8	1.51
Visintin et al. ¹³	17	150–171	0 or 2.85	Hooked or straight	35 or 13	0.55 or 0.2	75 × 75	16	3.57
Hung et al. ¹⁴	16	111–128	0 or 2	Hooked	30	0.38	150 × 150	15.9, 19.1, 22.2 or 25.4	0.88–2.25
Khorami et al. ¹⁵	36	139–154	1 or 2	Straight	13	0.2	60 × 60, 80 × 80 or 100 × 100	10 or 12	1.13–2.18

Note: *N*, number of tests; *f_c*, compressive strength; *V_f*, fiber volume; *l_f*, length of the fiber; *d_f*, fiber diameter; *d_b*, bar diameter; ρ , reinforcement ratio. Abbreviation: UHPFRC, ultra-high performance fiber reinforced concrete.

TABLE 2 Summary of geometric and material properties of UHPFRC pull-out tests

Reference	<i>N</i>	<i>f_c</i> (MPa)	<i>V_f</i> (%)	Fiber type	<i>l_f</i> (mm)	<i>d_f</i> (mm)	<i>c</i> (mm)	<i>d_b</i> (mm)
Reineck and Greiner (2004)	1	160	2	Straight	13	0.2	40	4
Jungwirth and Muttoni ¹¹	2	199	2.5	Straight	20	0.3	70–74	12 or 20
Oesterlee ¹²	6	155–219	0–3	Straight	13	0.16	21	8
Yoo et al. (2014)	6	185–207	1–4	Straight	13	0.2	67.1	15.9
Yuan and Graybeal (2014)	151	82–137	2	Straight	12.7	0.2	12.7–55.9	12.7 or 15.9 or 22.2
Alkaysi and El-Tawil ²⁰	6	191	2	Straight	19	0.2	65.5–68.5	13 or 16 or 19
Sturm and Visintin ¹⁹	21	150–171	0–2.85	Hooked or straight	35 or 13	0.55 or 0.2	25–75	16

Note: *N*, number of tests included in the database; *f_c*, compressive strength; *V_f*, fiber volume; *l_f*, length of the fiber; *d_f*, fiber diameter; *c*, cover; *d_b*, bar diameter. Abbreviation: UHPFRC, ultra-high performance fiber reinforced concrete.

In the remainder of the paper, the results of 12 pull-out test and 8 tension-stiffening tests conducted on specimens with large diameter (20 mm and 24 mm) bars are first presented. The pull-out test results are then combined with 203 existing results to allow the regression of a new τ_b - δ material model applicable to larger diameter bars. The τ_b - δ material property is then used as the basis for modifying an existing partial-interaction model for UHPFRC^{9,24} to allow for prediction of tension-stiffening, crack formation, and crack opening from first loading to reinforcement rupture.

2 | EXPERIMENTAL PROGRAM

2.1 | UHPFRC mix design

All test specimens are constructed using the same mix design and source materials as those used in Sturm et al.²⁵ The mix design presented in Table 3, for both ultra high performance concrete (UHPC) without fibers and UHPFRC with a 2% fiber volume is based on that of Sobuz et al.²⁶ and consists of sulphate-resisting cement and silica-fume as the binder and washed river sand as the filler. A third-generation high range water reducer is used to obtain a flowable mix. For the UHPFRC, straight steel fibers with a length of 13 mm, a diameter of 0.2 mm, and yield strength of 2850 MPa are used.

The UHPFRC was mixed in a pan mixer with a capacity of 500 L by first mixing the dry ingredients for 1 min. The water and superplasticizer were then added and the mortar mixed until visibly flowable, the steel fibers were then added and mixed for a further 5 min. The UHPFRC was placed starting from each end of the specimen mold and working toward the center. Rodding was used to ensure good compaction was achieved around the bars. It is expected that there was minimal disturbance of the fiber orientation as the minimum clear cover was 40 mm (three times the fiber length). After casting, the specimens were then allowed to cure for 7 days in their molds under wet hessian before being stored in ambient lab conditions until the time of testing.

TABLE 3 Mix design

	Unit weight (kg/m ³)	
	$V_f = 0\%$	$V_f = 2\%$
Cement	960	940
Silica fume	255	250
Sand	960	940
Water	182	179
Superplasticizer	43	42
Steel fibers	0	156

2.2 | Pull-out tests

Pull-out tests were conducted to quantify the bond between the reinforcement and the UHPFRC, with a particular focus on larger diameter bars (20 mm and 24 mm). To facilitate simple and rapid testing of a range of different covers for each bar diameter, the testing approach developed by Sturm and Visintin¹⁹ was applied. In this approach, a large block containing bars at a range of different covers is cast with sufficient distance between each bar to prevent interaction between individual tests. To complete the test program outlined in Table 4, three blocks were cast: one each of block type 1 and 2 in Figure 1a,b were cast using the UHPFRC and to allow for a simple comparison of the impact of fibers, an additional block type 1 was cast using UHPC without fibers.

The test specimens shown in Figure 1 have a depth of 220 mm and the bar is bonded over a distance shown in Figure 1c,d, with a polyvinyl chloride pipe used over the remaining length to break the bond. This very short bonded length is necessary in UHPFRC to ensure pull-out before yielding of the reinforcement. During testing, shown in Figure 1e, the bar is pulled using a hollow hydraulic ram, which reacts against the test specimen and a bolted reinforcing bar coupler. The load is applied using a hand jack at an approximate load rate of 30 kN/min until the peak load is reached, after which an approximate displacement rate of 4 mm/min is applied. Throughout testing, Linear Variable Differential Transformers (LVDTs) are used to measure the slip of the reinforcement at both the loaded and free end.

2.3 | Tension-stiffening tests

Tension-stiffening tests were conducted to quantify the elongation, crack-spacing, and crack-width from first loading until rupture of the reinforcement. To generate the experimental observations, eight tension ties with elevation shown in Figure 2a, and cross-section shown in

TABLE 4 Pull-out test specimen details

Test ID	V_f (%)	d_b (mm)	c (mm)
N20-50	0	20	40
N24-60	0	24	48
F20-50	2	20	40
F20-75	2	20	65
F20-100	2	20	90
F24-60	2	24	48
F24-90	2	24	78
F24-120	2	24	108

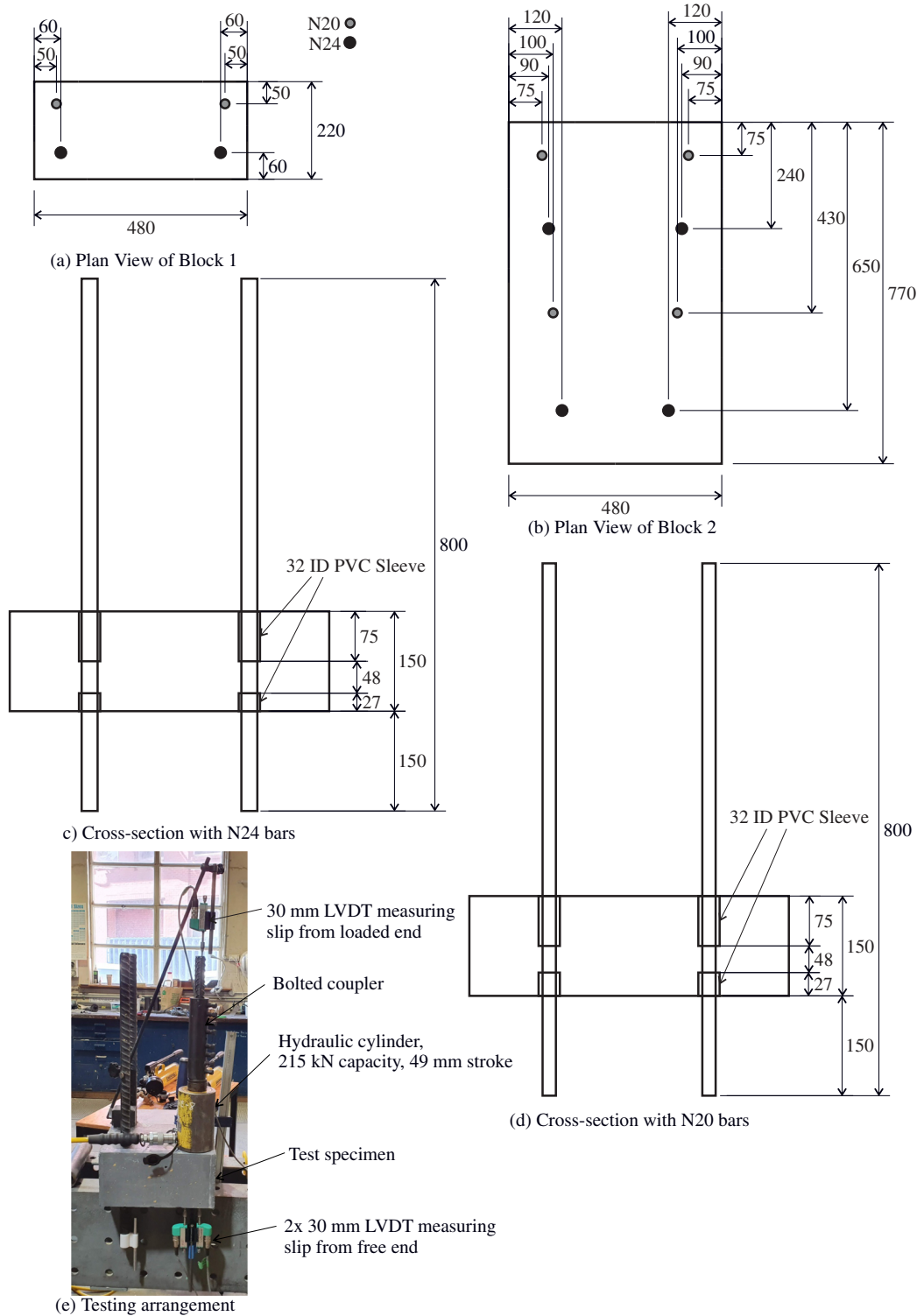


FIGURE 1 Details of pull-out specimens

Figure 2b were constructed. Specific details of each specimen are provided in Table 5. The bar diameter and cross-section were varied to investigate the effect of bar diameter and reinforcement ratio on tension-stiffening behavior. As a comparison to explore the influence of fibers, for one reinforcement ratio and two bar diameters, specimens with no fibers were tested.

To enable the investigation of post-yield behavior, the reinforcement in Figure 2a consisted of three portions: the test region of the bar which was of either 20 mm or 24 mm diameter and the two grip regions which consists of a 28 mm diameter bar which was joined to the test bar with a full-penetration butt weld. To prevent premature splitting failure at the location of the weld, the connection was provided with

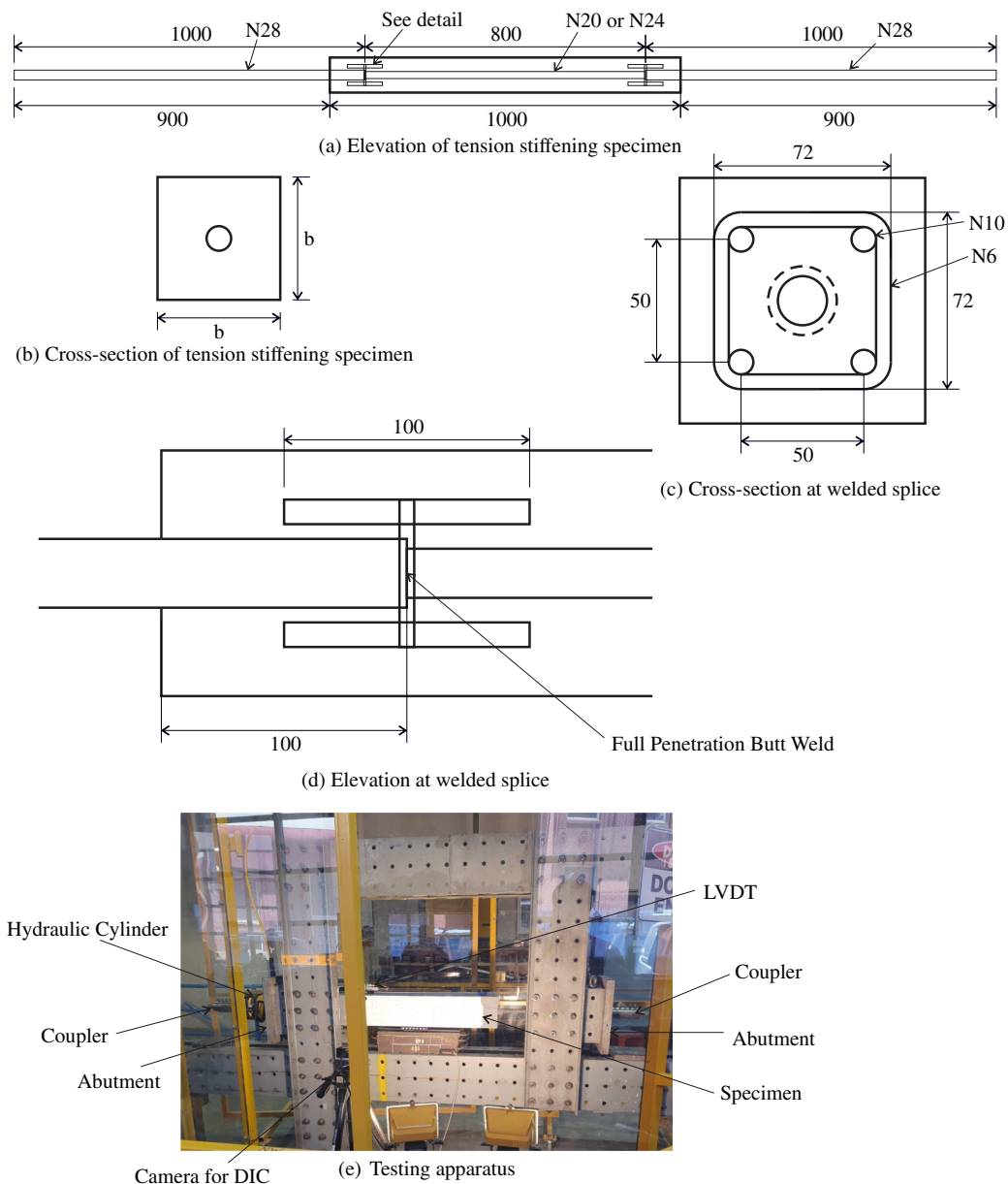


FIGURE 2 Tension-stiffening specimens

TABLE 5 Tension-stiffening specimen details

Test ID	V_f (%)	d_b (mm)	b (mm)	c (mm)	ρ (%)
N20-100	0	20	100	40	3.14
N24-120	0	24	120	48	3.14
F20-100	2	20	100	40	3.14
F20-150	2	20	150	65	1.40
F20-200	2	20	200	90	0.79
F24-120	2	24	120	48	3.14
F24-180	2	24	180	78	1.40
F24-240	2	24	240	108	0.79

additional reinforcement consisting of four 10 mm diameter bars contained within 6 mm stirrups as shown in Figure 2c,d.

For testing, the tension tie was mounted between two abutments; at the live-end the axial load was applied using a hollow hydraulic ram reacting between the abutment and a reinforcing bar coupler attached to the grip region, while at the dead-end a reinforcing bar coupler beared up against the abutment [see Figure 2e]. During testing, the specimens were loaded using a hand jack at an approximate load rate of 35 kN/min until yield, and then at a displacement rate of 5 mm/min until failure. Throughout testing, loads were measured using a

pressure transducer connected to the hydraulic cylinder. Elongation was measured using LVDTs mounted on the top and back surface of the specimen; the LVDT gauge length was taken to be 800 mm and aligned with region of the specimen containing the 20 mm or 24 mm bar. To enable detailed observation of crack formation and crack-widening, the front surface of the specimen was painted white and speckled so that images can be recorded using a black and white camera at a rate of 5 Hz. The images were then used to determine the surface strains using digital image correlation (DIC) software to detect cracks and measure crack-widths.

3 | RESULTS

3.1 | Concrete material properties

The compressive strength of the concrete was determined using 100 mm diameter cylinders of 200 mm height according to the standard procedure defined in AS1012.9²⁷ but in which the load rate was applied according to ASTM C1856.²⁸ Three compression tests were conducted at 28 days and at the time of testing of the tension-stiffening specimens. For the mix without fibers the average compressive strength was found to be 108 MPa at 28 days and 117 MPa at the time of tension-stiffening testing. For the mix with fibers, the average 28-day strength was 93 MPa and the strength at the time of tension-stiffening testing was 106 MPa.

An identical mix design was used by Sturm et al.²⁵ who reported direct-tensile stress–strain and stress–crack width behavior obtained from dog-bone shaped specimens with a cross-sectional area of 120 × 120 mm and a test region of length 300 mm. The stress–strain and stress–crack width relationships obtained from triplicates of testing are summarized in Figure 3.²⁵ For the mix with no fibers the tensile strength of the concrete is 3.74 MPa and the elastic modulus is 37.3 GPa.

To allow for the impact of time-dependent deformations on the tension-stiffening behavior, the concrete shrinkage strain was measured according to the procedure outlined in ASTM C157.²⁹ At the time of testing the shrinkage strain was 1089 $\mu\epsilon$ for the no fiber mix and 976 $\mu\epsilon$ for the fiber mix.

3.2 | Reinforcement material properties

The stress–strain relationship for a 20 and 24 mm reinforcing bar was obtained from direct tension tests in which the elongation of the bar was measured over a 50 mm gauge length using an extensometer. The stress–strain relationship of the reinforcing bars obtained is shown in

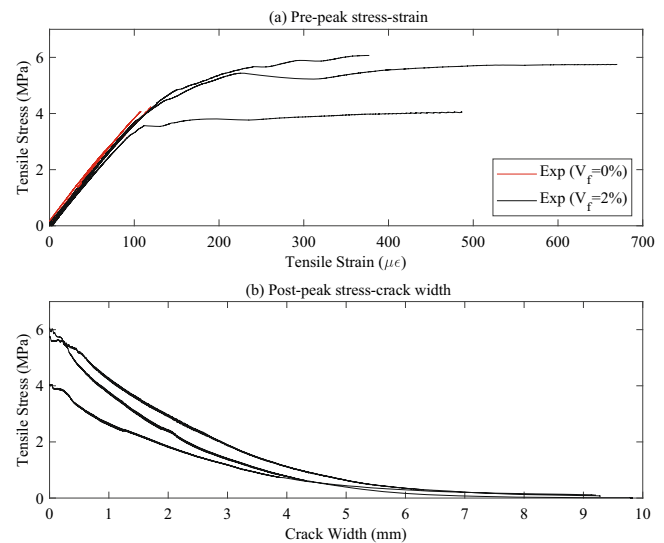


FIGURE 3 Tensile stress–strain and stress–crack width relationships

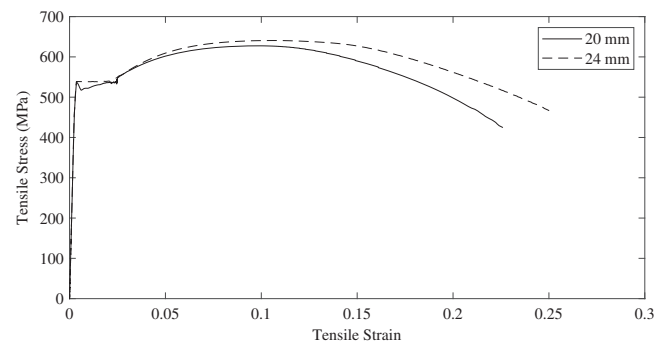


FIGURE 4 Stress–strain relationship of reinforcement of a 24 mm reinforcing bar

Figure 4. The 20 mm bar has a yield strength of 536 MPa and the 24 mm bar has a yield strength of 539 MPa. The 20 mm bar has an ultimate tensile strength of 628 MPa obtained at a strain of 0.098. The 24 mm bar has an ultimate tensile strength of 641 MPa at a strain of 0.107.

3.3 | Pull-out tests

The results of the pull-out tests are shown in Figure 4a–h. Comparing each set of test results, it can be seen that for specimens with fibers a decrease in bar diameter and an increase in cover results in a greater bond strength but otherwise the general shape of the τ_b – δ response is similar. The reason for the increase in bond strength with cover is that greater confinement of the reinforcing bar occurs due to the dilatancy of the concrete.³⁰ This variation with bar diameter indicates that a

size effect is present, and this size effect has been observed for bond in conventional concrete.^{23,31}

The specimens without fibers follow a similar trend to the specimens with fibers until splitting occurs, after which the bond rapidly reduced to zero. The rapid reduction in bond stress after the initiation of splitting cracks occurs because without fibers or coarse aggregates there are no mechanisms to transfer tensile stresses across the cracked plane. This was indicated in a recent study by Khaksefidi et al.³² where the bond of UHPC without fibers but with coarse aggregates was investigated and uncontrolled splitting was not observed, thereby indicating that coarse aggregates are also effective at restraining splitting in UHPC. As a result of the splitting failure of the specimens without fibers only three test results were obtained from the block without fibers.

An idealized bond stress–slip relationship shown in Figure 5, with the form described in Equation (1), was fit to all test results in Figure 6.

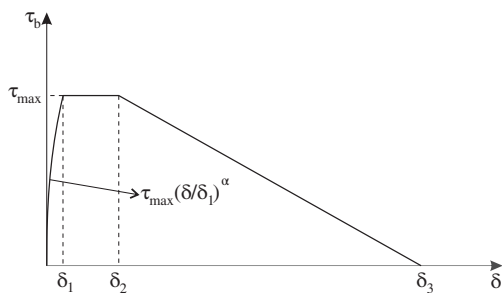


FIGURE 5 Idealized bond stress–slip relationship

$$\tau_b = \begin{cases} \tau_{max} \left(\frac{\delta}{\delta_1} \right)^\alpha; \delta > \delta_1 \\ \tau_{max}; \delta_1 < \delta < \delta_2 \\ \tau_{max} \frac{\delta_3 - \delta}{\delta_3 - \delta_2}; \delta_2 < \delta < 10 \text{ mm} \end{cases}, \quad (1)$$

where in Equation (1), τ_{max} is the peak bond strength, δ_1 is the initial slip at the peak bond strength, δ_2 is the final slip at the peak bond strength, δ_3 is the x -intercept to give the correct slope for the descending branch of the bond stress–slip relationship, and α is the exponent of the bond stress–slip relationship. The values for each of these key parameters resulting in the best fit to the test results are summarized in Table 6 while the fits themselves are shown in Figure 7.

To enable the calibration of a generalizable τ_b – δ relationship, these new test results for larger diameter bars were combined with 180 pull-out test results from the database in Sturm and Visintin.¹⁹ This database also included results from Reineck and Greiner,³³ Jungwirth and Muttoni,¹¹ Oesterlee,¹² Yoo et al.,³⁴ and Yuan and Graybeal.³⁵ In addition, new data from Alkaysi and El-Tawil²⁰ was added to the database. In compiling this database it is significant to note that while 195 test results provide data suitable to quantify the peak bond strength, only 30 tests (15.7% of the database) provide sufficient information to obtain the remaining parameters to fit Equation (1). It is therefore suggested that when conducting future research to quantify the bond between reinforcement and UHPFRC it is essential to measure both load and deformation and fully report this data.

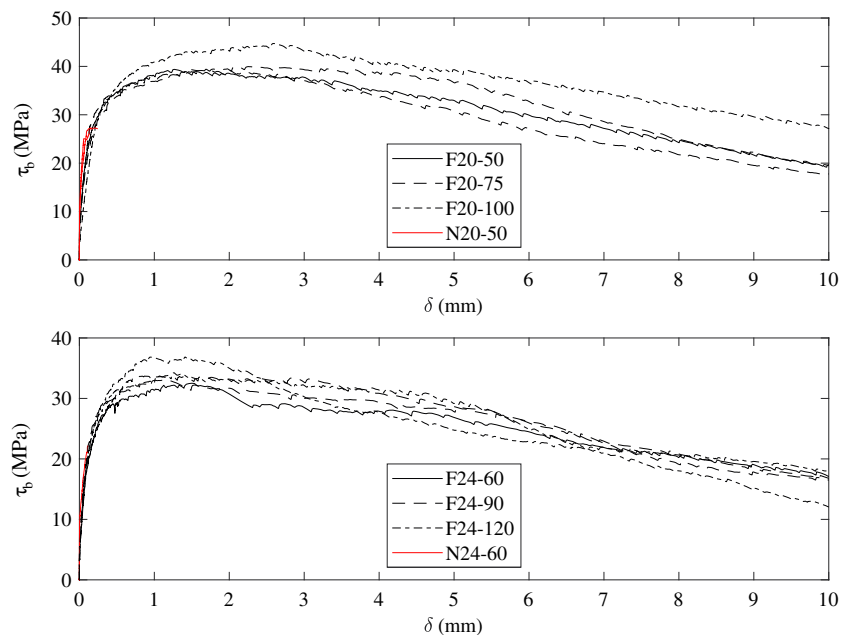


FIGURE 6 Pull-out test results

TABLE 6 Fitting results

V_f (%)	d_b (mm)	c (mm)	τ_{max} (MPa)	δ_1 (mm)	δ_2 (mm)	δ_3 (mm)	α
2	20	50	38.2	0.684	2.83	17.3	0.286
2	20	75	38.4	0.763	2.29	15.7	0.303
2	20	75	39.1	1.039	4.21	15.1	0.210
2	20	100	43.2	0.927	3.05	22.1	0.366
2	24	60	31.4	0.531	1.63	20.3	0.337
2	24	90	33.3	0.624	3.10	15.7	0.327
2	24	90	31.3	0.368	3.27	17.5	0.358
2	24	120	35.2	0.577	0.91	17.6	0.348
2	24	120	32.6	0.474	3.87	13.3	0.344
0	20	50	27.2	0.164			0.205
0	20	50	27.1	0.246			0.166
0	24	60	22.2	0.117			0.310

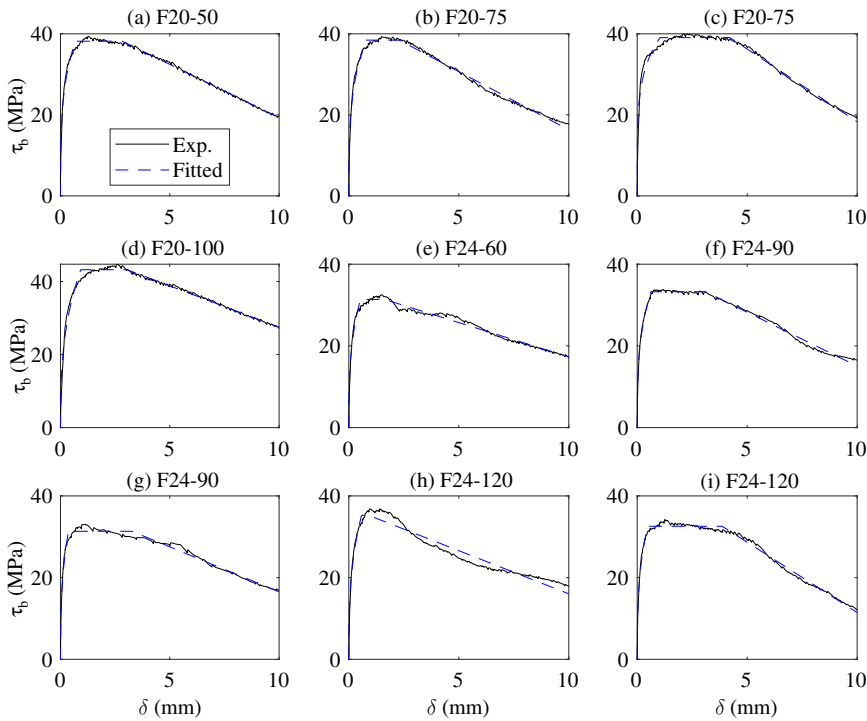


FIGURE 7 Fit of idealized bond stress-slip relationship

Conducting linear regression, the relationship between the key points of the τ_b - δ relationship and the reinforcement and concrete material properties and specimen geometry are given by

$$\tau_{max} = 0.143 f_c + 12.8 V_f - 0.495 d_b + 0.292 c - 17.8, \quad (2)$$

$$\delta_1 = 0.0441 d_b - 0.398, \quad (3)$$

$$\delta_2 = 2.09 \text{ mm}, \quad (4)$$

$$\delta_3 = 14.5 \text{ mm}, \quad (5)$$

$$\alpha = 0.404, \quad (6)$$

where f_c is the concrete strength. Equations (2)–(6) are valid for f_c between 82 and 219 MPa, V_f between 1% and 4%, d_b between 4 and 24 mm, and c between 12.7 and 108 mm.

For specimens without fibers, the behavior is assumed to be the same as for a specimen with fibers until splitting occurs. From the linear-regression analysis,

the bond stress at splitting based on the 15 test results in the database is

$$\tau_{sp} = 0.248f_c, \quad (7)$$

The summary statistics describing the goodness of fit of Equations (2)–(7) and the test data are provided in Table 7. Examining the parametric dependencies in

TABLE 7 Summary statistics

Exp./pred.	τ_{max}	δ_1	δ_2	δ_3	α	τ_{sp}
Mean	1.00	0.99	1.00	1.00	1.00	0.99
Std. dev.	0.18	0.47	0.43	0.19	0.23	0.25
COV	0.18	0.48	0.43	0.19	0.23	0.26
Max.	1.82	2.15	2.01	1.52	1.86	1.33
Min.	0.45	0.24	0.30	0.76	0.52	0.33

Equations (2)–(7), it can be seen that an increase in cover increases the peak bond strength and an increase in bar diameter increases the slip to reach the peak bond strength and decreases the peak bond strength. The other parameters that define the bond stress–slip relationship are unaffected by this variation in bar diameter or concrete cover. The increase of peak bond strength with cover is due to the confinement of the reinforcing bar and the decrease with bar diameter is due to the size effect. This size effect has also been observed in the bond of normal strength concrete by Ichinose et al.³¹ and Bamonte and Gambarova,³⁶ and can be explained by the fracture of the quasi-brittle concrete during pull out.³⁶ Quasi-brittle materials have a size effect because the size of the fracture process zone does not scale with the size of the specimen but rather is assumed to be a function of the microstructure.³⁷ The increase in slip at the peak bond strength indicates that there is a size effect for the bond stiffness as well.

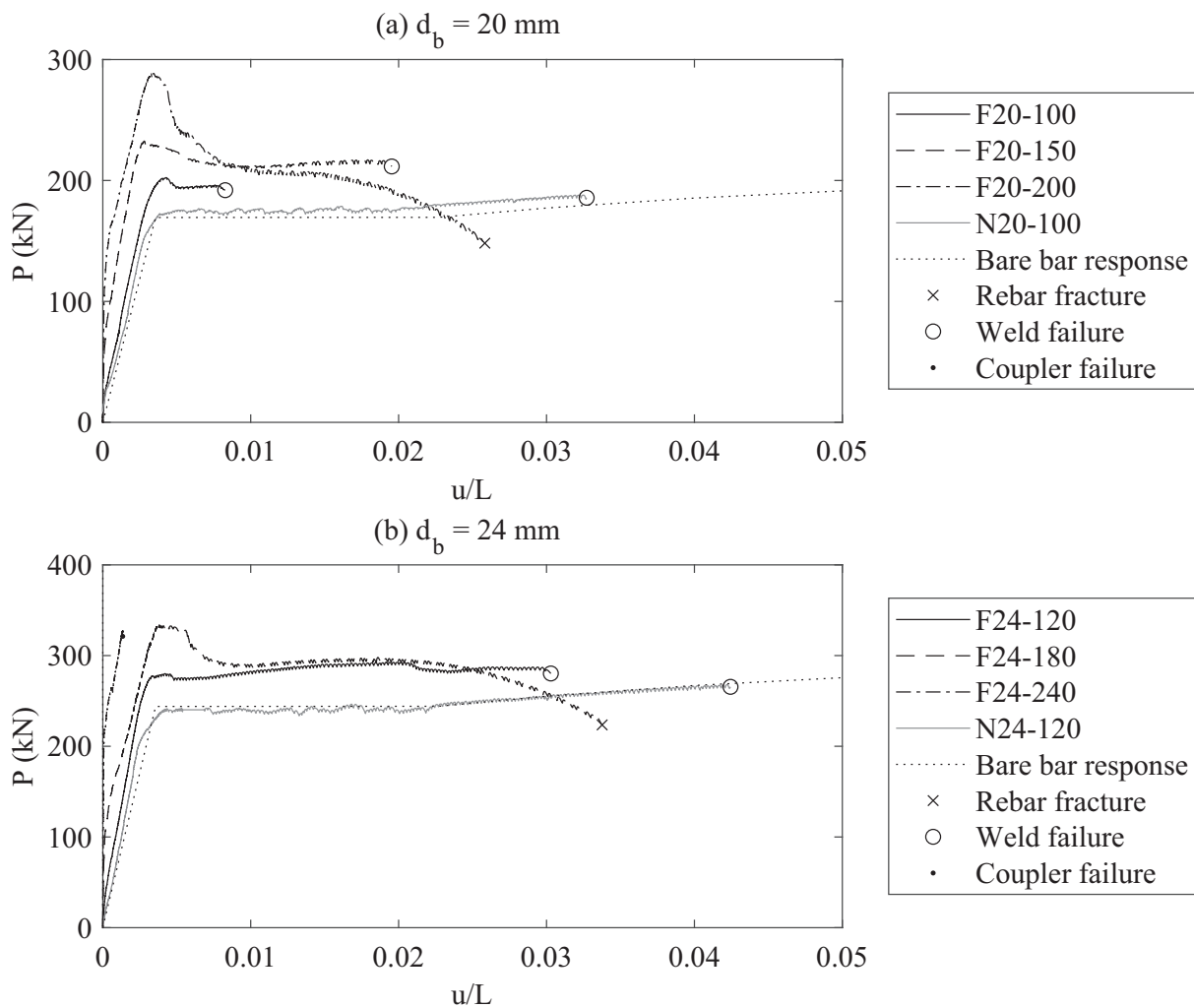


FIGURE 8 Effect of reinforcement ratio on tension stiffening

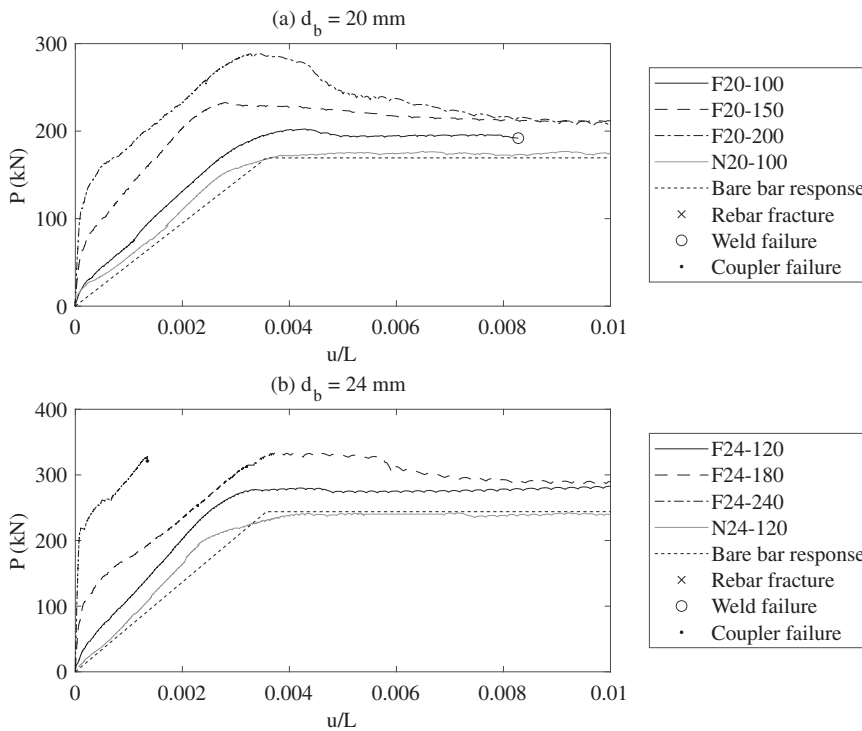


FIGURE 9 Effect of reinforcement ratio on tension stiffening (u/L up to 0.01)

TABLE 8 Peak load, elongation at peak load, and number of cracks

V_f (%)	b (mm)	d_b (mm)	P_{max} (kN)	u_{max} (mm)	u_{fr} (mm)	Failure mode
0	100	20	188	25.77		Failure of weld
2	100	20	202	3.42		Failure of weld
2	150	20	233	2.23		Failure of weld
2	200	20	289	2.75	21.5	Fracture of rebar
0	120	24	268	33.75		Failure of weld
2	120	24	293	15.33		Failure of weld
2	180	24	334	3.07	27.0	Fracture of rebar
2	240	24				Failure of coupler

Note: “Failure of weld” refers to fracture of the weld connecting the smaller and larger reinforcing bars. “Failure of rebar” refers to fracture of the reinforcement within the test region. “Failure of the coupler” refers to failure of the coupler which was transferring the load from the hydraulic cylinder into the specimen. After coupler failure slips, this slip limits the transfer of additional force to the specimen.

3.4 | Tension-stiffening tests

The measured load–average strain relationships obtained for each tension-stiffening test by dividing the LVDT elongation u by the gauge length L are shown in Figure 8, and are also compared to the stress–strain relationship of the bare bar. In Figure 9, a close up of the ascending part of the curve is given to show more detail. Furthermore, the peak loads P_{max} , elongation at peak load u_{max} , elongation at fracture of the reinforcement u_{fr} , the number of cracks N , and the average spacing S_{cr} are reported in Table 8. The failure mode of each specimen is also shown. From this it can be seen for six of the eight tests, failure was in the weld or the coupler, which should

be seen as a deficiency of the test setup; however, the results up until this point should still be considered valid. The final two failed within the specimen and these tests should be considered to be representative of the full range tension-stiffening behavior.

The results in Figure 8 show that the cracking load, stiffness, and strength of the section increases as the reinforcement ratio decreases. The magnitude of tension-stiffening can be seen in Figure 10, where the additional stress due to the tension stiffening σ_{ts} is plotted. This additional stress due to tension stiffening is calculated by taking the difference between the experimental force and the bare bar response for a given elongation and then dividing by the cross-sectional area of the specimen. No

FIGURE 10 Tension-stiffening stress

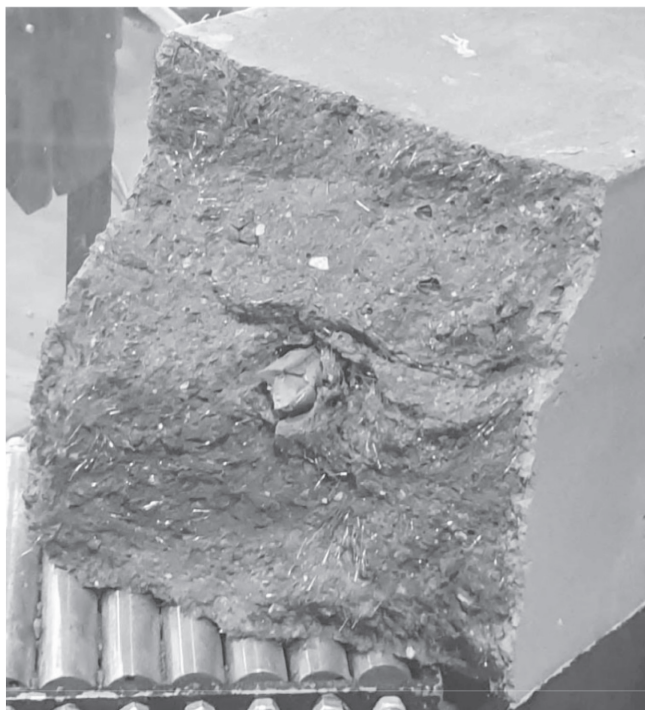
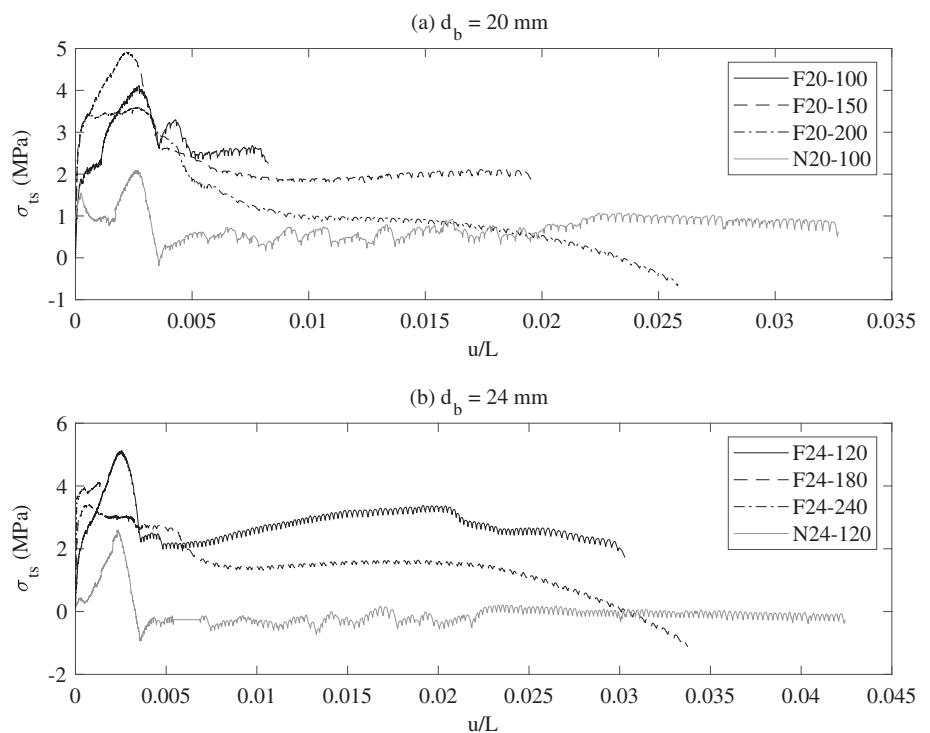


FIGURE 11 Failure surface for F24-180

clear trends are seen as a function of the reinforcement ratio. The variation seen is attributed to the variability of the tensile properties of the fibers evidenced by the direct tension tests in Figure 3. It is also seen that tension-stiffening is substantially greater for specimens with fibers. This is observed by noting that the peak tension-

stiffening stress for specimens without fibers is approximately 50% less than that of the equivalent specimen with a fiber volume of 2% for both bar diameters. This change in tension-stiffening is because of the contribution of the fibers bridging the cracks. That is, for UHPFRC, the average stresses in the concrete at the crack face is non-zero, while for concrete with no fibers, the stress at the crack face is zero. It is also seen that after yield, tension-stiffening of the specimens without fibers approaches zero. This is due to splitting of the cover concrete which reduces the bond stresses to nearly zero in specimens without fibers, after which the specimens acts as a bare bar. This behavior is further evidenced by the pull-out tests in Figure 6. The difference in tension-stiffening stress observed between N20-100 and N24-120 is likely due to specimen N24-120 being cracked as a result of restrained shrinkage prior to testing. Although these cracks were not visually observed, cracking is suspected to have occurred because the expected change in slope of the load–elongation relationship (Figure 8) that occurs as a result of first cracking is not observed.

In Figure 8, it is observed that the elongation at failure increases proportionally to the cross-section. It cannot however be established if this behavior is real or an artifact of the specimens with a reduced cross-section failing by fracturing of the weld, compared to the specimens with a larger cross-section (F20-200 and F24-180) where failure was via bar fracture in the test region. Necking was observed in specimens F20-200 and F24-180, with the failure surface of specimen F24-180 shown in

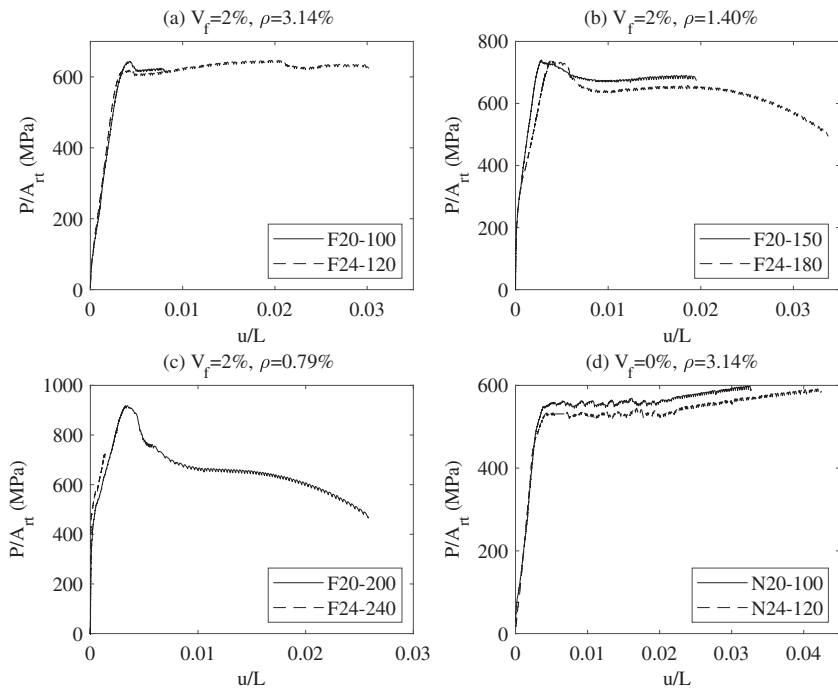


Figure 11. Specimen F24-240 was sufficiently strong such that the coupler failed before the specimen and hence only the initial portion of the ascending branch could be obtained. The effect of fibers on the elongation is observed by considering the elongations of N20-100 and N24-120 exceed that of F20-200 and F24-180 despite the fact the latter two failed by rupture of the reinforcement while the first two failed due to fracture at the weld. This behavior is a result of the post-yield elongation localizing to one crack for the specimens with fibers, while localization to one crack had not yet occurred for the specimens without fibers; it is hypothesized that this would not have occurred until the initiation of necking. The reason for this is that once the bar has yielded the increase of stress due to strain hardening of the reinforcement is slower than the decrease in stress due to the pullout of the fibers.

In Figure 12, the effect of bar diameter is shown; it can be seen that bar diameter has negligible effect on load–elongation behavior if the force is normalized by the area of the reinforcement for a given reinforcement ratio. The reason for this is that the force in the reinforcement is directly proportional to the area of reinforcement whereas the force in the concrete for a constant concrete stress is inversely proportional to the reinforcement ratio.

Let us now consider the results obtained from DIC. To verify the DIC measurements the elongation computed by the DIC is first compared to the elongation measured by the LVDTs. This elongation is measured using the virtual extensometer available in the DIC software. For F20-150 in Figure 13, it is seen that a close

FIGURE 12 Effect of bar diameter on tension stiffening

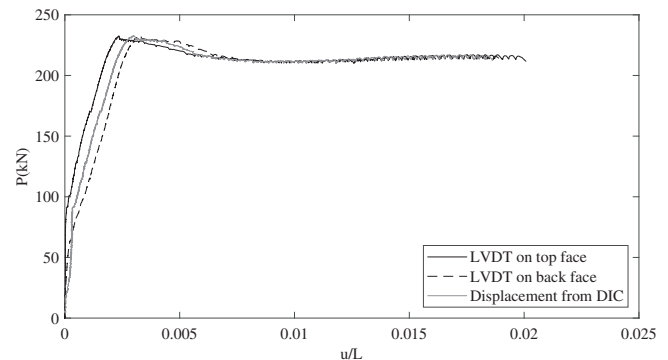


FIGURE 13 Comparison of deformation from DIC and LVDTs for F20-150. DIC, digital image correlation

correlation exists between the elongations obtained from the LVDTs and the DIC.

To illustrate the fracture patterns, longitudinal surface strains are shown for each specimen at peak load in Figure 14 (note that the DIC results could not be resolved for N24-120) where the regions of elevated strain correspond to cracks. Here, cracks are shown at the peak load since this is when the majority of the cracks are at their largest size and therefore the most visible. As the load decreases post-yield all cracks begin to close except the largest crack, which is that which causes failure of the specimen.

Comparing the results in Figure 14a,b which are obtained from specimens that are identical except for the fiber content, the influence of fibers on crack formation can be seen. While for the specimens without fibers the

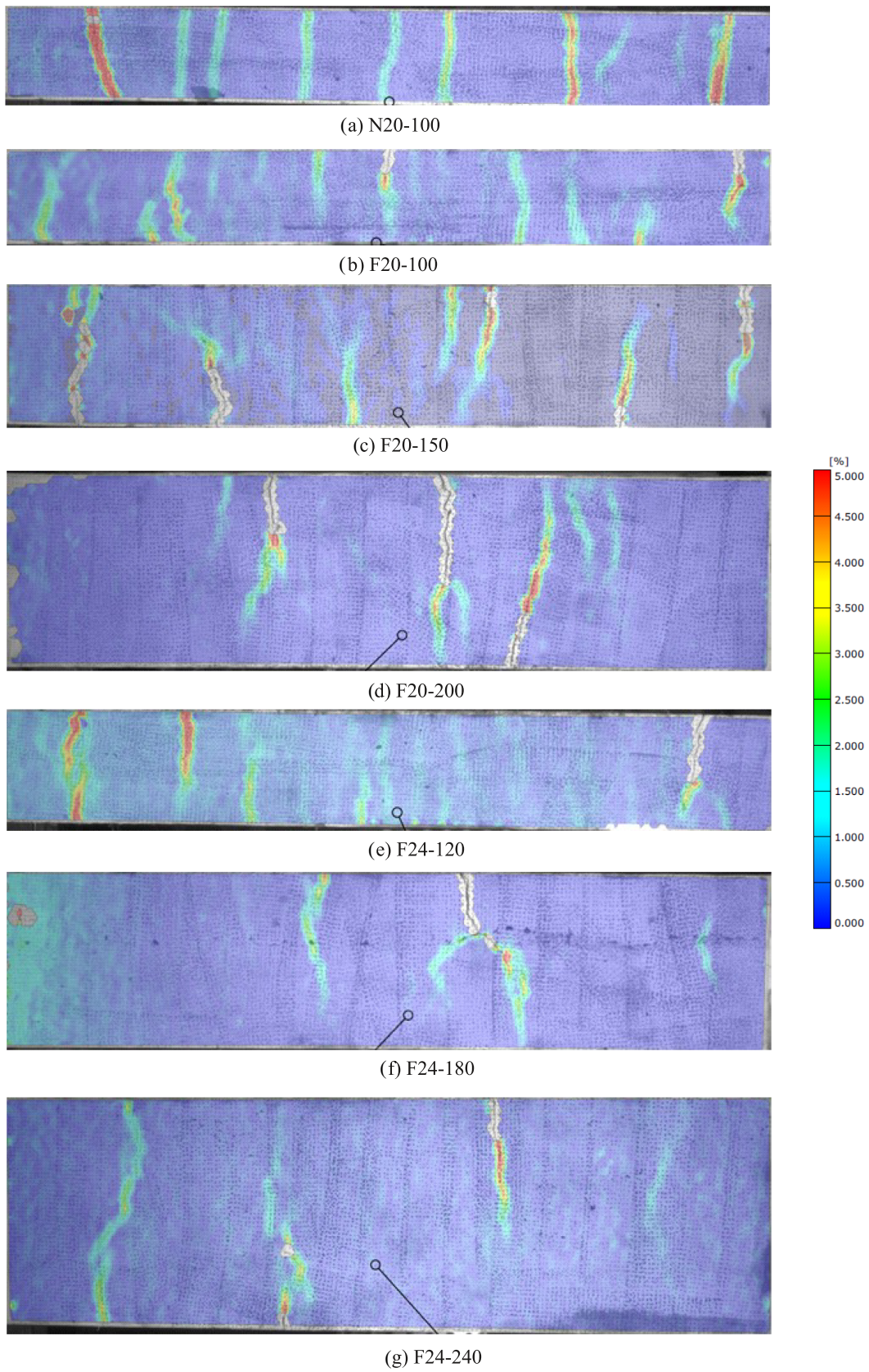


FIGURE 14 Longitudinal surface strains at the peak load

majority of the cracks extend across the entire section at regular spacing, for the specimen with fibers, the crack pattern is more complex and irregular. Most cracks are seen to initiate from a corner and do not extend across the whole section; in general, only the crack that causes the failure of the specimen propagates across the whole section. The termination of cracks along the specimen depth is likely a result of the local variation in tensile properties arising from the local distribution of fibers.

It can also be observed that the geometry of the cracks when fibers are present is often more complex, for example see the branching paths in F24-180 in Figure 14f. This is likely due to the local distribution of fibers influencing the direction of the crack as it propagates through locally weak sections.

For all specimens with fibers, microcracking is observed; for example, considering specimen F24-120 shown in Figure 14e, it is seen that there are three large cracks at the left-hand side of the specimen and one large crack at the right. However, in between there appears to be many small discontinuous fractures indicating microcracking. This variation of large distinct cracks in some sections and small discontinuous cracks was also observed in Sturm et al.⁸ in pretensioned flexural members. It is hypothesized that this related to the inconsistent strain hardening of the UHPFRC observed during the direct tension tests conducted in Visintin et al.¹³ where some specimens from the same mix would display substantial strain hardening or none at all. Li and Leung³⁸ have suggested that the transition between strain hardening and non-strain hardening behavior is a function of the crack-tip and fiber bridging toughness as well as the size of flaws within the specimen. If the initial flaws are too small or this ratio is too large than strain hardening will not occur. The spatial variation of these properties would result in this inconsistent behavior where strain hardening occurs in some regions and not others. This variation is also observed in Figure 3a and supports the need to conduct direct-tension tests on specimens with large cross-section such that a more realistic variation in tensile behavior is observed, rather than on thin specimens as suggested by JSCE³⁹ and Graybeal and Baby⁴⁰ in which the cross-section dimensions forces preferential orientation of fibers and therefore an upper bound estimation of the tensile response.

The surface strains at failure measured by the DIC where rupture of the reinforcement occurred within the specimen test region are shown in Figure 13. It is observed that when failure occurs via reinforcement rupture one very large crack extends across the entire section with the remaining cracks either stabilizing or reducing in width. The reason for this is that the

elongation localizes to one crack after the peak load is reached (at yield for specimens with fibers). After this point, as a result of the relatively low strain hardening modulus, the additional force contributed by the reinforcement is less than that lost by the fiber reinforcement as they pull out along the falling branch of the stress-crack width relationship in Figure 3.

The software used for DIC analysis also allows for the quantification of displacements using virtual extensometers placed on the specimen. A virtual extensometer was placed across the crack identified to cause failure, and the resulting load/maximum crack-width behavior is plotted in Figures 15 and 16. The maximum crack-width is considered here, because due to the complex crack geometry it is unclear where the crack widths should be measured to give a representative average reading. Hence, the maximum crack-width, which is also critical for design, is presented instead.

From Figure 16 it can be seen that generally the maximum crack-width for a given load increases with increasing reinforcement ratio. This is because for a given crack-width, a greater force is carried by the fibers in specimens with a smaller reinforcement ratio because of the greater cross-sectional area of concrete. This trend is only violated by F20-200 where the maximum crack-width was greater at some loads than for F20-150 which may be due to the variation in tensile properties due to the fibers. The difference in maximum crack-width was however larger for the specimens with 24 mm bars. It was also found that for the specimens without fibers that the crack width was substantially larger for a given force which is again due to the additional force due to the fibers not being present. The first cracking load for N20-100 is additionally observed to be very small due to the effect of the restrained shrinkage.

In Figure 17, it is observed that for the same reinforcement ratio the crack widths are substantially larger for specimens with larger diameter reinforcing bars. This could be due to the increased bar diameter increasing the crack spacing. That is, as the bonded perimeter reduces for a larger diameter bars in comparison to the area of reinforcement a longer length is required to transfer sufficient force into the concrete to cause cracking if the reinforcement ratio is held constant.

For the two specimens where failure occurred within the specimen, it is seen that the maximum crack-width is approximately 15 mm at the initiation of necking for F20-200 and 22 mm at the rupture of the reinforcement. Similarly, for F24-150 the maximum crack width is 18 mm and the crack width at the rupture of the reinforcement is 26 mm. It is inconclusive whether this difference is due to an increase in bar diameter or the difference in reinforcement ratio.

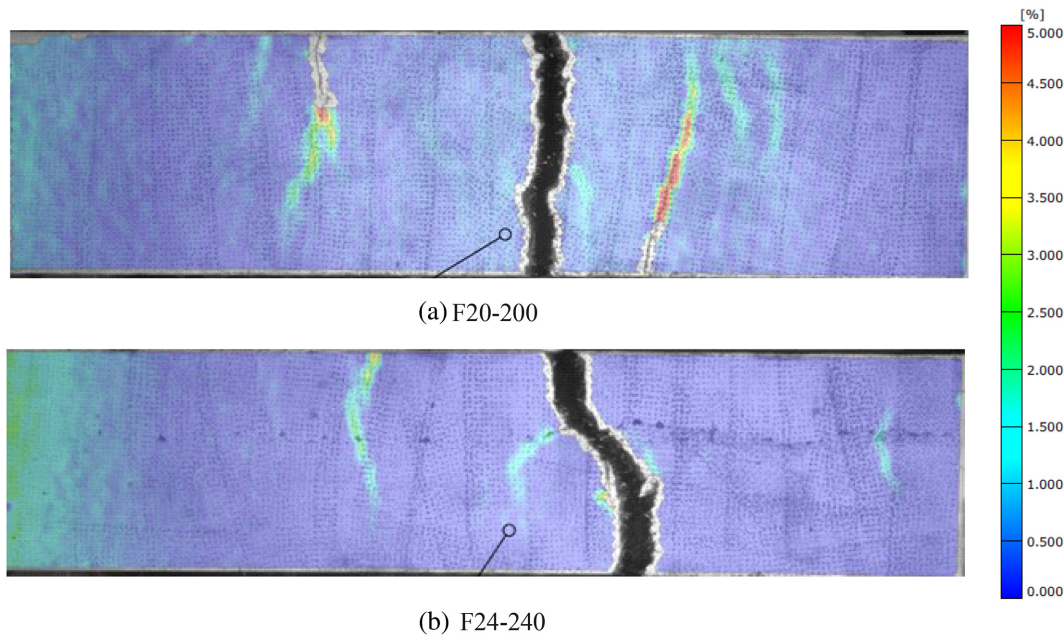
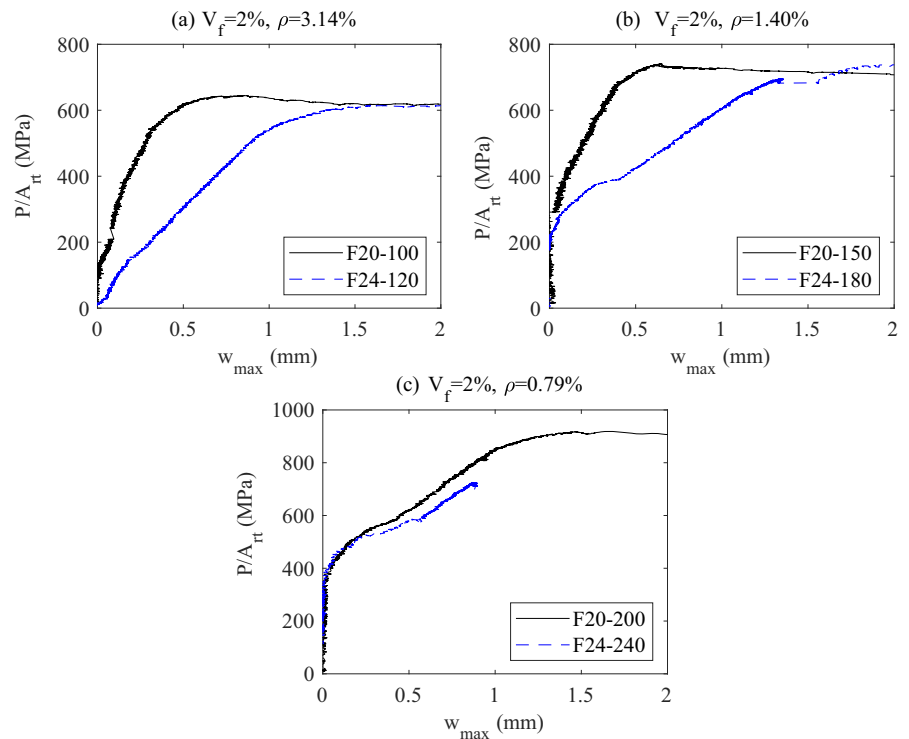


FIGURE 15 Surface strains at failure

FIGURE 16 Maximum crack widths (sorted by bar diameter)



4 | TENSION-STIFFENING ANALYSIS

To enable prediction of the experimental results a numerical partial-interaction model developed by Sturm et al.⁹ which was previously used to simulate UHPFRC flexural members is implemented. The same underlying mechanics were also applied to develop closed form solutions for

predicting the behavior of tension chords in Sturm et al.²⁴ but the numerical implementation is considered here so that post-yield behavior can be studied. Full details of the numerical model can be found in Sturm et al.⁹ and so only an overview necessary for the extension to post-yielding behavior is presented here.

First, consider the pre-cracking force–strain relationship as shown in Figure 18a, with the first point

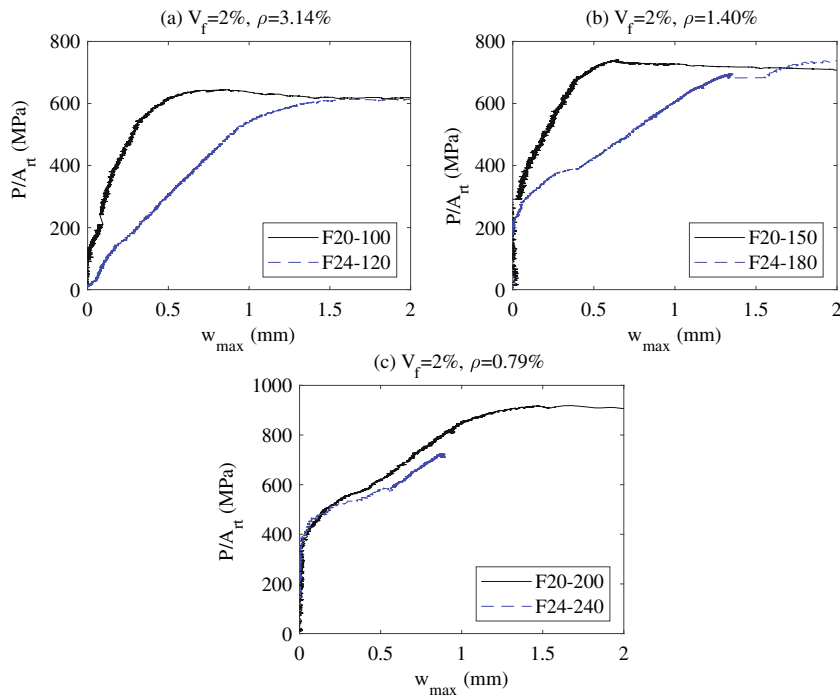


FIGURE 17 Maximum crack widths (sorted by reinforcement ratio)

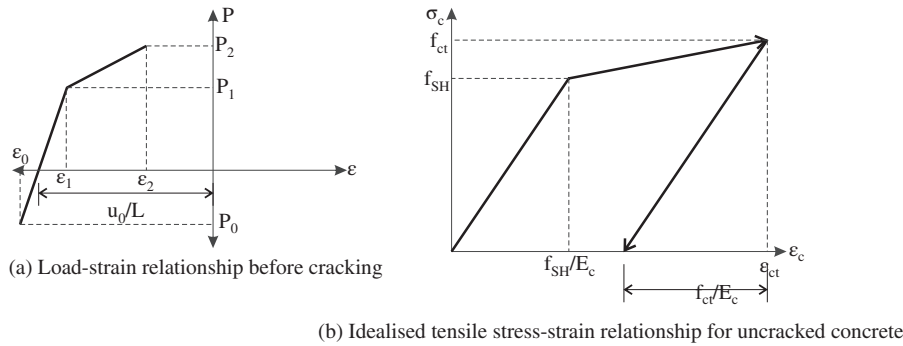


FIGURE 18 Load-strain and stress-strain relationships for uncracked concrete

corresponding to zero stress in the concrete. As the strain in the reinforcement is equal to the strain in the concrete minus the shrinkage strain, this first point is given by

$$\epsilon_0 = -\epsilon_{sh}, \quad (8)$$

and the corresponding load is

$$P_0 = -E_r A_{rt} \epsilon_{sh}, \quad (9)$$

where ϵ_{sh} is the shrinkage strain, E_r is the elastic modulus of the reinforcement, and A_{rt} is the area of the tensile reinforcement.

At the initiation of micro-cracking the strain in the concrete is

$$\epsilon_1 = \frac{f_{SH}}{E_c} - \epsilon_{sh}. \quad (10)$$

And the corresponding load in the concrete is

$$P_1 = E_r A_{rt} \epsilon_1 + f_{SH} A_{ct}, \quad (11)$$

where f_{SH} is the stress at the initiation of strain hardening in the tension response of the UHPFRC as shown in the idealized stress-strain relationship in Figure 18b, E_c is the elastic modulus of the concrete, and A_{ct} is the area of concrete in the tension chord.

After the formation of micro-cracks, the strain and force in the concrete at the initiation of macro-cracking is

$$\epsilon_2 = \epsilon_{ct} - \epsilon_{sh}, \quad (12)$$

$$P_2 = E_r A_{rt} \epsilon_2 + f_{ct} A_{ct}, \quad (13)$$

where ϵ_{ct} is the strain in the concrete at the initiation of macro-cracking and f_{ct} is the tensile strength of the concrete.

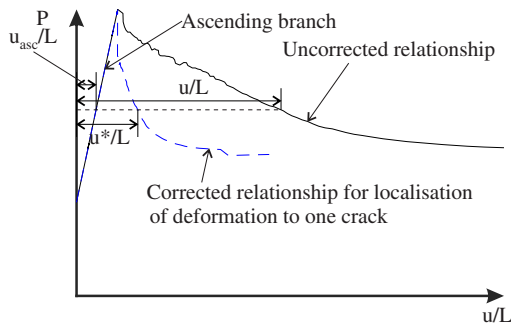


FIGURE 19 Tension chord

Having described the pre-cracking behavior, the post-cracking behavior is now derived by considering the tension-chord illustrated in Figure 19a,b, in which the crack-spacing (Equation (14)) is defined using the analytical expression derived in Sturm et al.²⁴ using identical partial-interaction mechanics.

$$S_{cr} = \left[\frac{2^\alpha(1+\alpha)}{\lambda(1-\alpha)^{1+\alpha}} \right]^{\frac{1}{1+\alpha}} \left[\frac{f_{ct} - f_{pc}}{E_c} \left(\frac{E_c A_{ct}}{E_r A_{rt}} + 1 \right) \right]^{\frac{1-\alpha}{1+\alpha}}, \quad (14)$$

in which,

$$\lambda = \frac{\tau_{max}}{\delta_1^\alpha} L_{per} \left(\frac{1}{E_r A_{rt}} + \frac{1}{E_c A_{ct}} \right), \quad (15)$$

and f_{pc} is the fiber stress at the crack face. L_{per} is the bonded perimeter of the reinforcement while τ_{max} , δ_1 , and α are defined by the bond material model developed earlier.

To determine the corresponding load–crack width for this tension-chord, the stress in the reinforcement at the crack face σ_{rt} is imposed and the crack width w is guessed; the slip of the reinforcement relative to the concrete at the crack face at the crack face $\delta(0)$ is taken as half the crack-width. The guess for the crack width corresponding to an imposed reinforcement stress is correct when the slip at the mid-span $\delta(S_{cr}/2)$ is equal to zero. From σ_{rt} the force in the reinforcement at the crack face $P_r(0)$ can be determined. The crack width w allows the stress f_{pc} in the fibers at the crack face to be determined from the experimental tensile stress–crack width relationships in Figure 1b, and knowing the stress in the concrete the concrete force $P_c(0)$ is also known.

The magnitudes of the reinforcement force P_r , concrete force P_c , and slip δ at all points along the tension chord are illustrated in Figure 15c–e. The fields of force and displacement in Figure 17 can be obtained by solving

the following system of three first-order differential equations, where Equations (16) and (17) are from longitudinal equilibrium and Equation (18) is from compatibility

$$\frac{dP_r}{dx} = -\tau_b L_{per}, \quad (16)$$

$$\frac{dP_c}{dx} = \tau_b L_{per}, \quad (17)$$

$$\frac{d\delta}{dx} = \varepsilon_r - \varepsilon_c + \varepsilon_{sh}, \quad (18)$$

in which the bond stress τ_b is as a function of the slip δ and is defined by the material τ_b – δ relationship, the strain in the reinforcement ε_r is a function of the force in the reinforcement P_r as given by the stress–strain relationship in Figure 4 and the strain in the concrete ε_c is

$$\varepsilon_c = \varepsilon_{ct} - \frac{f_{ct}}{E_c} + \frac{\sigma_c}{E_c} = \varepsilon_{ct} - \frac{f_{ct}}{E_c} + \frac{P_c}{E_c A_{ct}}. \quad (19)$$

As UHPFRC displays a strain hardening tensile behavior it is assumed that the entirety of the uncracked concrete is loaded to a stress of f_{ct} and a strain of ε_{ct} as shown in Figure 18b before the first macro-crack forms. As evidenced by tests from Wille et al.⁴¹ if the UHPFRC is unloaded from this point the stress–strain relationship does not follow the initial curve and instead unloads from this point with some unloading modulus hence some of this strain is permanent and unrecoverable. To represent this behavior, the stress–strain relationship of the UHPFRC after the formation of the first macro-crack is assumed to follow Equation (19). For simplicity this unloading modulus has assumed to be equal to the initial elastic modulus as was done in Sturm et al.^{8,9,24} where it was found that this assumption did not influence the accuracy of the predictions. This simplification is implemented as it removes the need to determine the unloading modulus experimentally.

Solving for P_r , P_c , and δ at each point along the tension-chord using Equations (16)–(18), the slip at the center of the tension chord $\delta(S_{cr}/2)$ can be determined and by applying the boundary condition that at the center of the chord the slip must be zero, the guess for the crack width w can be updated. Once the boundary condition is satisfied, the crack width w corresponding to the stress in the reinforcement σ_{rt} has been determined and the corresponding load in the tension chord is

$$P = P_r(0) + P_c(0). \quad (20)$$

The overall elongation of the specimen can be determined by integrating the reinforcement strains over the length of the specimen between the two points where the elongation is measured. If the elongation is then normalized by the length of the specimen, the mean reinforcement strain is

$$\frac{u}{L} = \frac{\int_0^L \epsilon_r dx}{L} = \bar{\epsilon}_r. \quad (21)$$

For comparison to the experimental results, Equation (22) needs to be corrected to allow for the fact that the initial

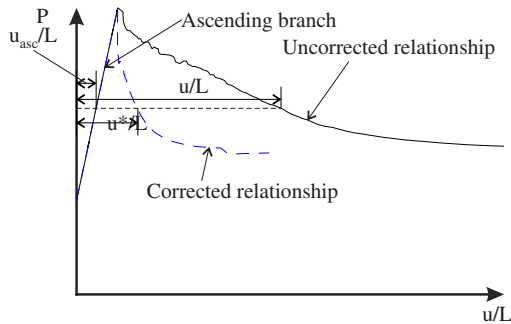


FIGURE 20 Correction for descending branch of load-elongation relationship

length for the analytical approach is the length before shrinkage, whereas experimentally the initial length for the elongation measurement is the length after shrinkage has occurred. To do this the corrected elongation $\frac{u^*}{L}$ is taken as

$$\frac{u^*}{L} = \frac{u}{L} - \frac{u_0}{L}, \quad (22)$$

where u_0/L is the elongation of the specimen when the force in the tension chord P is 0 as shown in Figure 15a.

A further correction needs to be provided for the case where the peak load is reached before necking has occurred. The reason for this is that while the derived elongation-load relationship is valid for a specimen with one crack, for a specimen with multiple cracks only one of the cracks will follow the descending branch. The other cracks are taken to instead follow the initial ascending relationship and begin to close. This behavior was observed in the presented tests, as there is one single large crack at failure as shown in Figure 15. If this effect is ignored the overall elongation of the specimen is overestimated. Hence, the correction is

$$\frac{u^*}{L} = \frac{u}{L} \left(\frac{S_{cr}}{L} \right) + \frac{u_{asc}}{L} \left(1 - \frac{S_{cr}}{L} \right), \quad (23)$$

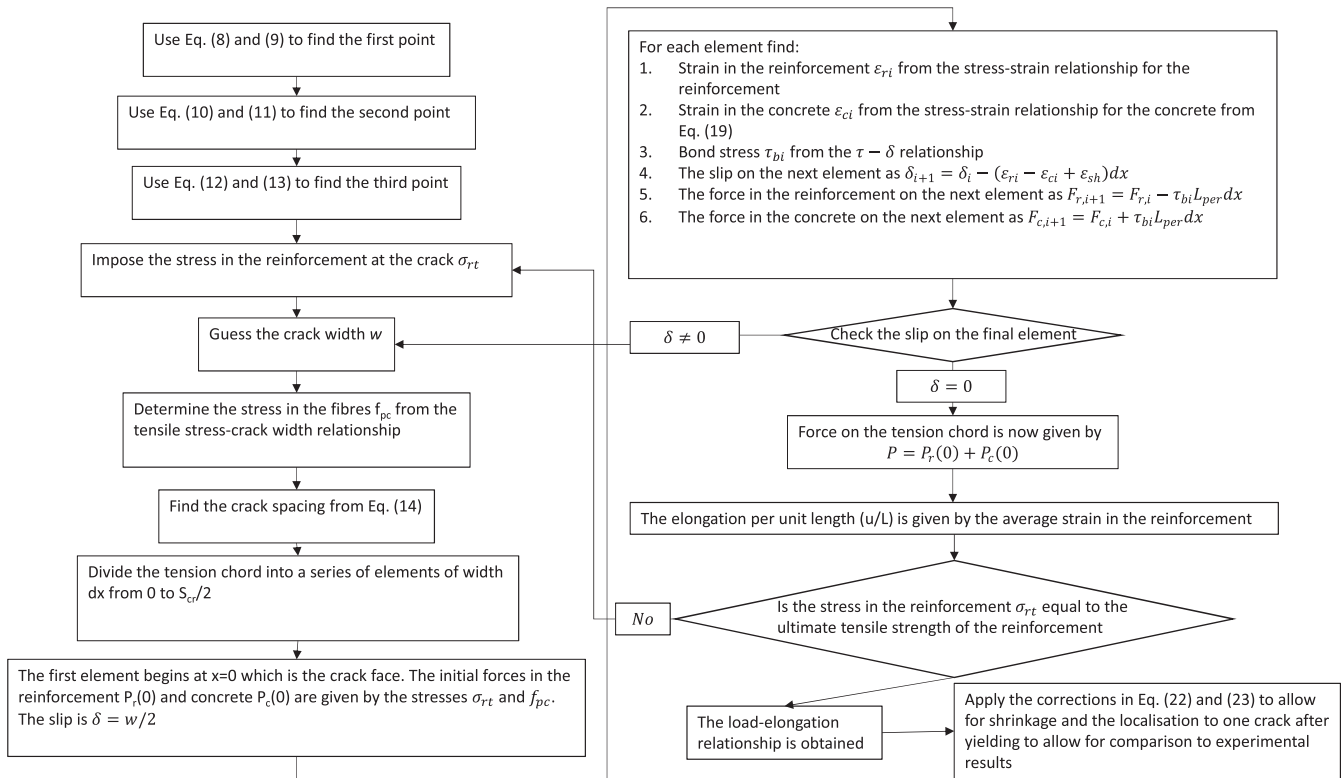
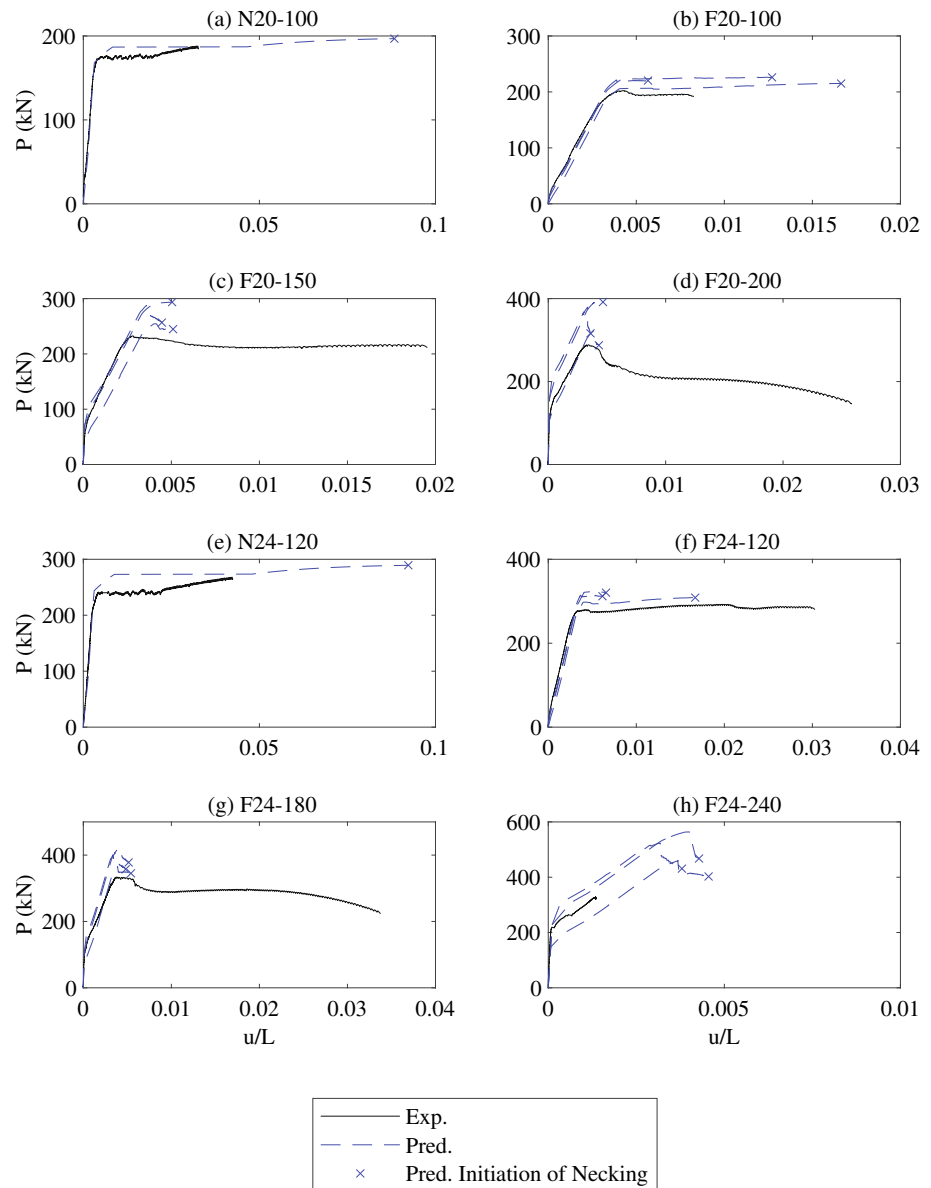


FIGURE 21 Flow chart for determining the load-elongation

FIGURE 22 Validation of analysis procedure



where S_{cr} is the crack spacing, L is the length over which the elongation is measured, and u_{asc}/L is the elongation for the same load but on the ascending branch where this is illustrated in Figure 20. Equation (23) essentially states that the uncorrected elongation is applied over one crack spacing while the elongation of the rest of the specimen matches the ascending branch. The procedure for determining the load-elongation is summarized in the flow chart in Figure 21.

In Figure 22, the analytical procedure is validated against the experimental results. It can be seen that for each specimen three predicted curves are presented, with each being obtained using a different replicate of the tensile stress-crack width relationships (Figure 3b). This approach was taken because the scatter in tensile stress-crack width behavior is the main contributor to the variability in the predicted load-elongation relationships.

From the comparison of predicted and experimental results it can be seen that the model fits well on the rising branch which matches the portion of the load-elongation relationship explored in Sturm et al.²⁴ However, when considering specimens F20-200 and F24-180 in Figures 22d,g which failed by fracture of the bar within the specimen test region, it can be seen that the model cannot capture the descending branch of the load-elongation relationship. The reason for this is that the bond properties have been assumed to be independent of strain in the reinforcement. For ordinary reinforced concrete it is well established that the bond reduces after the yield of the reinforcement as evidenced by the bond material model in the fib Model Code 2010¹⁷ including a yield factor. Hence, in the next section, a bond factor is introduced which is calibrated using the experimental results. In Figure 22a,e it is also observed that the fit

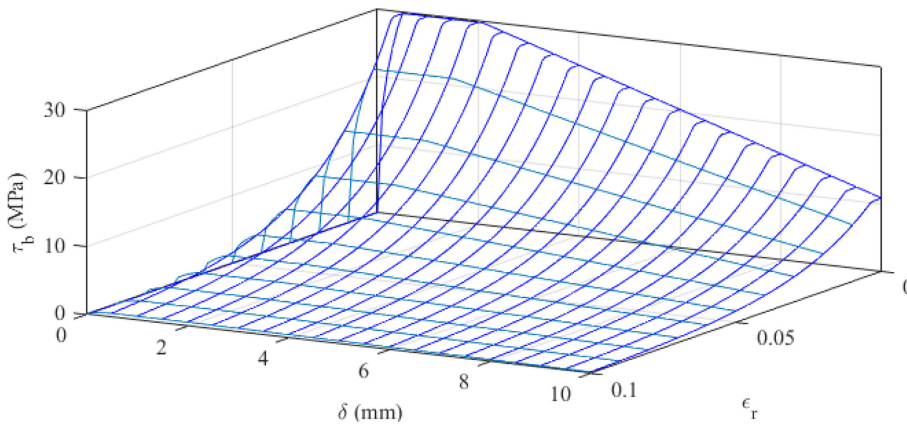


FIGURE 23 Bond stress–slip relationship with bond factor ($f_c = 106$ MPa, $c = 50$ mm, $d_b = 20$ mm)

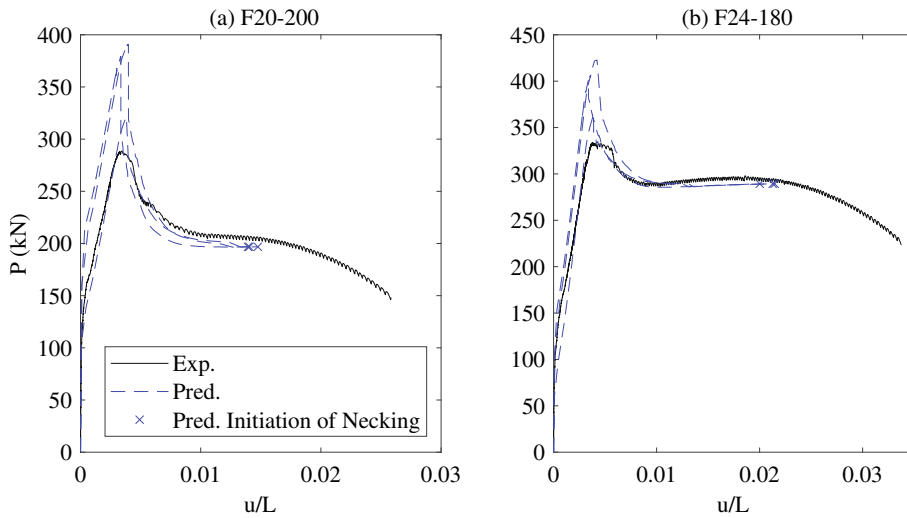


FIGURE 24 Calibration of bond yield factor Ω_y

obtained through modeling is better for specimens without fibers (N20-100 and N24-120) because splitting occurred before yielding.

4.1 | Effect of yield

To allow for the effect of yield, the bond properties are modified to

$$\tau_b^* = \begin{cases} \Omega_y \tau_b; \varepsilon_r > \varepsilon_y \\ \tau_b; \varepsilon_r < \varepsilon_y \end{cases}, \quad (24)$$

where τ_b is given by Equation (1) and the yield factor is

$$\Omega_y = \exp [A(\varepsilon_y - \varepsilon_r)], \quad (25)$$

in which ε_r is the strain in the reinforcement and ε_y is the yield strain and the resulting bond stress–slip relationship is illustrated in Figure 23.

The form of Equation (25), is taken from work by Ruiz et al.⁴² on conventional concrete, in which A is recommended to be 10. The A parameter was recalibrated for UHPFRC using the load–elongation for F20-200 and F24-180, where the best fit was found with an A of 45 for the 20 mm bar and 40 for the 24 mm bar as shown in Figure 24. In Figure 24 the impact of the variation in tensile stress/crack-width behavior is also shown by repeating the modeling with each of the three experimental tensile material properties. The recalibration of parameter A allowed the prediction of the descending portion of the load–elongation relationship up until the initiation of necking. After this point the prediction becomes more difficult as the length over which the necking occurs is required. Analysis to include the impact of necking was not pursued as the prediction of the behavior after necking is of little practical importance given the rate at which member failure occurs beyond this point.

The pre- and post-yield predicted load–elongation for all specimens with fibers is shown in Figure 25. From this comparison it can be seen that including the effect of yield allows the post-peak behavior to be predicted with

FIGURE 25 Validation of analysis with bond factor

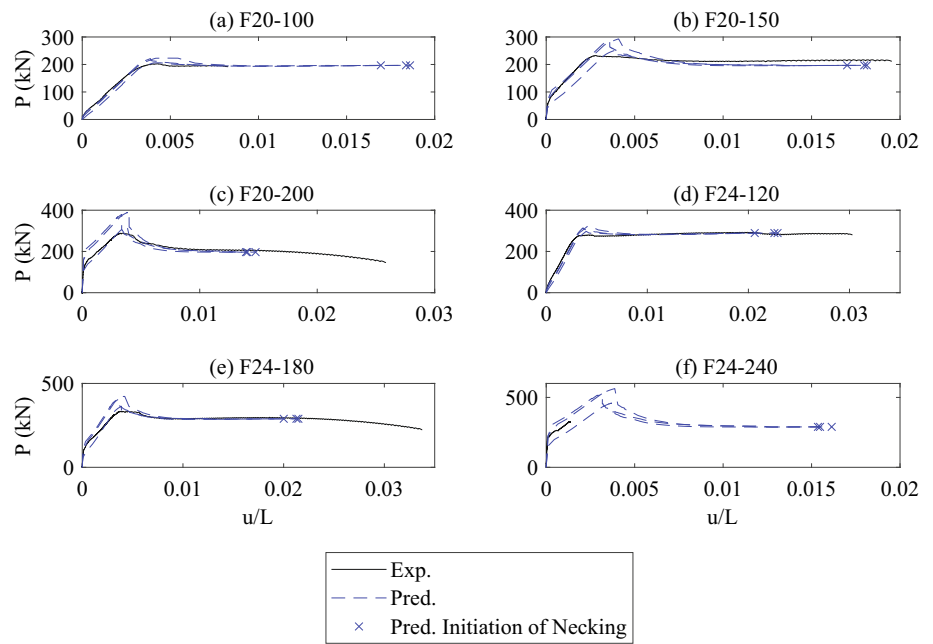
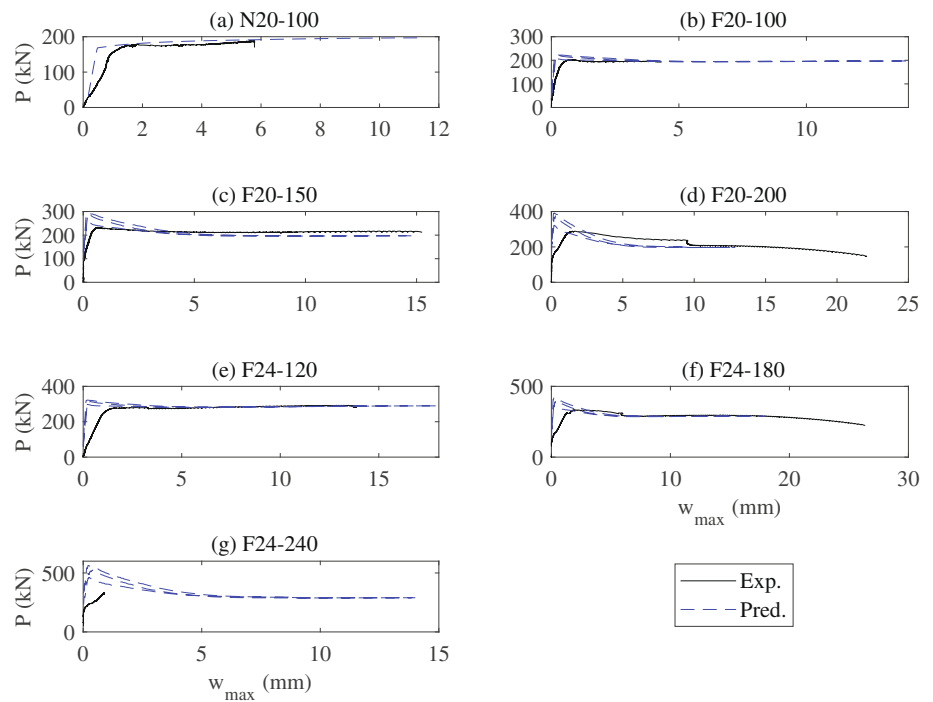


FIGURE 26 Comparison to crack widths



significantly improved accuracy. It is however, noted that the experimental maximum load most closely corresponds to the load–elongation predicted using the minimum tensile properties. The reason for this is that the strength of the tension specimens is controlled by the weakest cross-section since this is where the critical crack occurs. This suggests that the pre-peak response can be predicted using the mean stress/crack-width material properties but the maximum load should be predicted using properties corresponding to a lower bound.

4.2 | Comparison to crack widths

In Figure 26 the measured maximum crack-widths are compared to those obtained analytically. From this comparison it can be seen that after the peak, the predicted crack widths are similar to the experimental values, however pre-peak the experimental maximum crack-widths are overestimated. This outcome is consistent with the pre-peak behavior being driven by the mean response of the specimen while the post-peak behavior is dominated

by the weakest cross-section. Hence it can be concluded that the model yields an average crack-width for the pre-peak and a maximum crack-width for the post-peak loading.

Based on a statistical analysis, Deluce et al.⁴³ has suggested that for fiber-reinforced concretes, the ratio of the maximum to the mean crack-width is given by

$$\frac{w_{max}}{w_{mean}} = 1.7 + 3.4V_f \frac{l_f}{d_f}, \quad (26)$$

where l_f is the length of fiber and d_f is the diameter of the fiber. Equation (26) was derived with fibers of a length between 30 and 50 mm and aspect ratios of between 48 to 79 and therefore the fibers used in the study are outside of this length range but are within this aspect ratio range. Despite being outside the length range, the fit of Equation (26) to the current data suggests that it is in the range of applicability and can be extended to cover these fibers. For the specimens tested here, when the fiber volume is zero w_{max}/w_{mean} is 1.7 and when the fiber volume is 2% w_{max}/w_{mean} is 6.12. The result of implementing this correction between the maximum and mean crack-width is shown in Figure 27 where it is seen to improve the accuracy of predictions. Note that the minimum tensile properties gave the best predictions of the maximum crack width for five of the seven specimens with fibers, which suggests that the maximum crack-width is controlled by the minimum rather than the mean tensile properties. This approach was also found to

give an accurate prediction of the crack-width for the specimen without fibers. A comparison is also provided to the provisions for FRC in Standards Australia,¹⁸ where it was found that the code predictions were in the same range as the predicted values from the approach in this paper.

5 | CONCLUSION

This paper presents a series of 12 pull-out and 8 tension-stiffening tests where the fiber volume, reinforcement ratio, and bar diameter was varied. The new pull-out tests results were added to a database of 180 existing results and used as the basis for the regression of a new τ_b - δ material model UHPFRC. The results of the experimental pull-out tests found that the maximum bond stress increased with increasing cover while the slip to reach the peak bond stress increased with increasing bar diameter. From the tension stiffening tests it was found that decreasing the reinforcement ratio while holding the area of reinforcement constant substantially increased the strength, stiffness, and load at first cracking for UHPFRC tension members. However, it was also found that for the same reinforcement ratio, changing the bar diameter had no significant effect on the load-elongation behavior. As expected, fibers were found to increase the strength and stiffness.

A DIC system was used to investigate the fracture and post-cracking behavior of the UHPFRC tension-stiffening

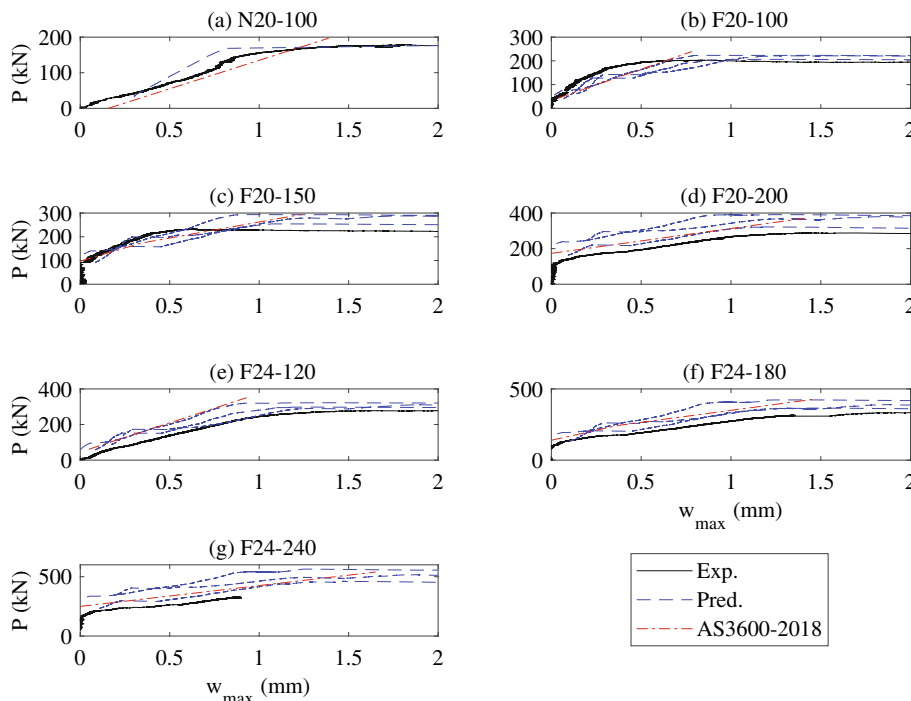


FIGURE 27 Comparison to pre-peak crack widths

specimens. From these experiments it was found that the specimens without fibers formed a regular crack pattern with cracks extending across the full depth of the specimen. For specimens with fibers, an irregular crack pattern occurred and often only the crack which caused the failure of the specimen extended across the full depth of the section. From the DIC results the maximum crack-widths were determined and it was found that for five of the specimens, crack-widths increased with increasing reinforcement ratio. It was also found that the fibers reduced the maximum crack-width. Increasing bar diameter substantially increased the maximum crack-width for specimens with reinforcement ratios of 1.40% and 3.14%.

The analysis approach developed in Sturm et al.²⁴ and Sturm et al.⁹ was then applied to predict the experimental results. It was found that this approach could accurately predict the pre-peak load–elongation as has been demonstrated in the previous studies; however, it could not accurately determine the post-peak response for specimens with fibers because it does not allow for the post-yield reduction in bond stress. To correct this, the bond was reduced post-yield by implementing and recalibrating the approach suggest by Ruiz et al.⁴²

With the bond reduced after yield according to this parameter it was found that accurate predictions of the post-peak response were obtained. Of particular importance, it was found that the mean tensile properties controlled the pre-peak behavior but the peak load and the post-peak behavior were controlled by the minimum tensile stress/crack-width properties. This indicates the importance in practice of performing sufficient testing to obtain a lower bound to the tensile stress/crack-width behavior in addition to the mean values.

Finally, the model was also applied to be predict the maximum crack widths. It was found that the model could accurately predict the crack widths post-peak as the response of the section was controlled by the maximum crack width. However, to obtain accurate predictions of the maximum crack width before the peak load it was found that the results from the model needed to be multiplied by a factor relating the mean to maximum crack width from Deluce et al.⁴³ This was originally developed for normal strength FRC, however, it was found to be applicable to UHPFRC as well.

ACKNOWLEDGMENTS

This material is based upon work supported by the Australian Research Council Discovery Project 190102650.

DATA AVAILABILITY STATEMENT

The data that support the findings of this study are available from the corresponding author upon reasonable request.

ORCID

Alexander B. Sturm  <https://orcid.org/0000-0001-5881-5112>


Phillip Visintin  <https://orcid.org/0000-0002-4544-2043>

NOTATION

A	rate of decrease for bond after yield
A_{ct}	cross-sectional area of tension chord
A_{rt}	cross-sectional area of reinforcement
b	width of tension-stiffening specimen
c	concrete cover
d_b	bar diameter
d_f	fiber diameter
E_c	elastic modulus of concrete
E_r	elastic modulus of reinforcement
f_{ct}	tensile strength of concrete
f_{pc}	stress in fibers at crack face
f_{SH}	stress in concrete at microcracking
L	gauge length for elongation measurement
L_{per}	bonded perimeter of reinforcement
l_f	length of fiber
N	number of cracks
P	load
P_c	force in concrete
P_{max}	peak load for tension-stiffening specimen
P_r	force in reinforcement
P_0	load when the stress in concrete is zero
P_1	load when concrete microcracks
P_2	load at cracking
S_{ave}	average crack spacing
S_{cr}	crack spacing
u	elongation
u^*	corrected elongation
u_{asc}	elongation on ascending branch of load–elongation relationship
u_{fr}	elongation at fracture
u_{max}	elongation at peak load
u_0	elongation when force is equal to zero
V_f	fiber volume
w	crack width
w_{max}	maximum crack width
w_{mean}	mean crack width
x	longitudinal position with respect to the crack face
α	exponent of bond stress–slip relationship
Δ	slip at crack face
δ	slip
δ_1	initial slip at maximum bond stress
δ_2	final slip at maximum bond stress
δ_3	intercept with horizontal axis for the bond stress–slip relationship
ε_c	strain in reinforcement
ε_{ct}	cracking strain

ε_r	strain in reinforcement
$\bar{\varepsilon}_r$	mean strain in reinforcement
ε_{sh}	shrinkage strain
ε_y	yield strain of reinforcement
ε_0	strain in reinforcement when stress in concrete is zero
ε_1	strain in reinforcement when stress in concrete initiates microcracking
ε_2	strain in reinforcement when concrete cracks
λ	tension stiffening parameter
ρ	reinforcement ratio of tension chord
σ_{ts}	tension-stiffening stress
τ_b	bond stress
τ_b^*	bond stress incorporating the effect of yield
τ_{max}	maximum bond stress
τ_{sp}	splitting bond stress
Ω_y	yield bond factor

ORCID

Alexander B. Sturm  <https://orcid.org/0000-0001-5881-5112>

Phillip Visintin  <https://orcid.org/0000-0002-4544-2043>

REFERENCES

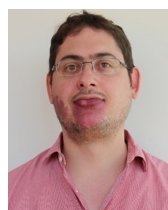
- Balazs GL. Cracking analysis based on slip and bond stresses. *ACI Mater J.* 1993;90(4):340–8.
- Marti P, Alvarez M, Kaufmann W, Sigrist V. Tension chord model for structural concrete. *Struct Eng Int.* 1998;8(4):287–98.
- Yankelevsky DZ, Jabareen M, Abutbul AD. One-dimensional analysis of tension stiffening in reinforced concrete with discrete cracks. *Eng Struct.* 2008;30(1):206–17.
- Borosnyói A, Balázs GL. Models for flexural cracking in concrete: the state of the art. *Struct Concr.* 2005;6(2):53–62.
- Lee SC, Cho JY, Vecchio FJ. Model for post-yield tension stiffening and rebar rupture in concrete members. *Eng Struct.* 2011;33(5):1723–33.
- Bischoff PH. Effects of shrinkage on tension stiffening and cracking in reinforced concrete. *Can J Civ Eng.* 2001;28(3):363–74.
- Gilbert RI. Tension stiffening in lightly reinforced concrete slabs. *J Struct Eng.* 2007;133(6):899–903.
- Sturm AB, Visintin P, Seracino R, Lucier GW, Oehlers DJ. Flexural performance of pretensioned ultra-high performance fibre reinforced concrete beams with CFRP tendons. *Compos Struct.* 2020a;243:112223.
- Sturm AB, Visintin P, Oehlers DJ. Blending fibres to enhance the flexural properties of UHPFRC beams. *Constr Build Mater.* 2020b;244:118328.
- Moreno DM, Trono W, Jen G, Ostertag C, Billington SL. Tension stiffening in reinforced high performance fiber reinforced cement-based composites. *Cem Concr Compos.* 2014;50:36–46.
- Jungwirth J, Muttoni A. Structural behavior of tension members in ultra high performance concrete. In: Schmidt M, Fehling E, Geisenhanslüke C, editors. *Proc. Int. Symp. On ultra high performance concrete.* Kassel, Germany: University of Kassel; 2004. p. 533–44.
- Oesterlee C. Structural response of reinforced UHPFRC and RC composite members. Ph.D. thesis. Lausanne, Switzerland: Ecole Polytechnique Federale de Lausanne; 2010.
- Visintin P, Sturm AB, Mohamed Ali MS, Oehlers DJ. Blending macro- and micro-fibres to enhance the serviceability behaviour of UHPFRC. *Aust J Civ Eng.* 2018;16(2):106–21.
- Hung CC, Lee HS, Chan SN. Tension-stiffening effect in steel-reinforced UHPC composites: constitutive model and effects of steel fibers, loading patterns, and rebar sizes. *Compos Part B Eng.* 2019;158:269–78.
- Khorami M, Navarro-Gregori J, Serna P. Tensile behaviour of reinforced UHPFRC elements under serviceability conditions. *Mater Struct.* 2021;54(1):1–17.
- CEN (European Committee for Standardization). (1992). *Design of concrete structures – Part 1-1: general rules and rules for buildings.* Eurocode 2, Brussels, Belgium.
- fib (International Federation for Structural Concrete). *CEB-FIP Model Code 2010.* Switzerland: Lausanne; 2013.
- Standards Australia (2018). *Concrete structures.* AS3600:2018. Sydney.
- Sturm AB, Visintin P. Local bond slip behaviour of steel reinforcing bars embedded in UHPFRC. *Struct Concr.* 2019;20(1):108–22.
- Alkaysi M, El-Tawil S. Factors affecting bond development between ultra high performance concrete (UHPC) and steel bar reinforcement. *Constr Build Mater.* 2017;144:412–22.
- Marchand P, Baby F, Khadour A, Battesti T, Rivillon P, Quierant M, et al. Bond behaviour of reinforcing bars in UHPFRC. *Mater Struct.* 2016;49(5):1979–95.
- De Larrard F, Shaller I, Fuchs J. Effect of the bar diameter on the bond strength of passive reinforcement in high-performance concrete. *ACI Mater J.* 1993;90(4):333–9.
- Soroushian P, Choi KB. Local bond of deformed bars with different diameters in confined concrete. *ACI Struct J.* 1989;86(2):217–22.
- Sturm AB, Visintin P, Oehlers DJ, Seracino R. Time dependent tension stiffening mechanics of fibre reinforced and ultra-high performance fibre reinforced concrete. *J Struct Eng.* 2018;144(8):04018122.
- Sturm AB, Visintin P, Oehlers DJ. Mechanics of shear failure in fiber-reinforced concrete beams. *J Struct Eng.* 2021;147(3):04020344.
- Sobuz HR, Visintin P, Ali MM, Singh M, Griffith MC, Sheikh AH. Manufacturing ultra-high performance concrete utilising conventional materials and production methods. *Constr Build Mater.* 2016;111:251–61.
- Standards Australia. (2000). *Methods of testing concrete – Compressive strength tests – Concrete, mortar and grout specimens.* AS 1012.9. Sydney.
- ASTM (American Society of Testing and Materials). *Standard practice for fabricating and testing specimens of ultra-high performance concrete.* ASTM C1856-17. Pennsylvania: West Conshohocken; 2017a.
- ASTM (American Society of Testing and Materials). *Standard test method for length change of hardened hydraulic-cement mortar and concrete.* ASTM C157-17. Pennsylvania: West Conshohocken; 2017b.
- Tastani SP, Pantazopoulou SJ. Direct tension pullout bond test: experimental results. *J Struct Eng.* 2010;136(6):731–43.

31. Ichinose T, Kanayama Y, Inoue Y, Bolander JE Jr. Size effect on bond strength of deformed bars. *Constr Build Mater.* 2004; 18(7):549–58.
32. Khaksefidi S, Ghalehnovi M, De Brito J. Bond behaviour of high-strength steel rebars in normal (NSC) and ultra-high performance concrete (UHPC). *J Build Eng.* 2021;33: 101592.
33. Reineck KH, Greiner S. Tests on ultra-high performance fibre reinforced concrete designing hot-water tanks and UHPFRC-shells. In: Schmidt M, Fehling E, Geisenhanslücke C, editors. *Proceeding of the International Symposium on Ultra High Performance Concrete.* Kassell, Germany: University of Kassell, 2004. p. 361–374.
34. Yoo DY, Shin HO, Yang JM, Yoon YS. Material and bond properties of ultra high performance fiber reinforced concrete with micro steel fibers. *Compos Part B Eng.* 2014;58:122–133.
35. Yuan J, Graybeal BA. Bond behavior of reinforcing steel in ultra-high performance concrete, No. FHWA-HRT-14-090. Mclean, VA: Federal Highway Administration, 2014.
36. Bamonte PF, Gambarova PG. High-bond bars in NSC and HPC: study on size effect and on the local bond stress-slip law. *J Struct Eng.* 2007;133(2):225–34.
37. Bazant ZP. *Scaling of structural strength.* 2nd ed. Burlington, Massachusetts: Elsevier; 2005.
38. Li VC, Leung CK. Steady-state and multiple cracking of short random fiber composites. *J Eng Mech.* 1992;118(11):2246–64.
39. JSCE (Japan Society of Civil Engineers). (2008). Recommendations for design and construction of high performance fiber reinforced cement composites with multiple fine cracks (HPRCC). *Concr Eng Ser.* 82.
40. Graybeal BA, Baby F. Development of direct tension test method for ultra-high-performance fiber-reinforced concrete. *ACI Mater J.* 2013;110(2):177.
41. Wille K, El-Tawil S, Naaman AE. Properties of strain hardening ultra high performance fiber reinforced concrete (UHP-FRC) under direct tensile loading. *Cem Concr Compos.* 2014; 48:53–66.
42. Ruiz MF, Muttoni A, Gambarova PG. Analytical modeling of the pre-and postyield behavior of bond in reinforced concrete. *J Struct Eng.* 2007;133(10):1364–72.
43. Deluce JR, Lee SC, Vecchio FJ. Crack model for steel fiber-reinforced concrete members containing conventional reinforcement. *ACI Struct J.* 2014;111(1):93.

AUTHOR BIOGRAPHIES



Alexander B. Sturm, Assistant Professor
Department of Civil Engineering,
National Cheng Kung University,
Tainan 70101, Taiwan (R.O.C.)
Email: asturm@gs.ncku.edu.tw



Phillip Visintin, Associate Professor
School of Civil, Environmental and
Mining Engineering, The University of
Adelaide, Adelaide, South Australia
5005, Australia
Email: phillip.visintin@adelaide.edu.au

How to cite this article: Sturm AB, Visintin P. Pre- and post-yield bond, tension-stiffening, and cracking in ultra-high performance fiber reinforced concrete. *Structural Concrete.* 2023;24(1):1201–25. <https://doi.org/10.1002/suco.202100711>